

EVALUATION OF TRIBOLOGICAL RESPONSE OF MOLYBDENUM DISULPHIDE-
BASED COATINGS TO VARYING ENVIRONMENTS

By

MATTHEW A. HAMILTON

A DISSERTATION PRESENTED TO THE GRADUATE SCHOOL
OF THE UNIVERSITY OF FLORIDA IN PARTIAL FULFILLMENT
OF THE REQUIREMENTS FOR THE DEGREE OF
DOCTOR OF PHILOSOPHY

UNIVERSITY OF FLORIDA

2007

© 2007 Matthew A. Hamilton

For Hobbes

ACKNOWLEDGMENTS

I would like to thank Dr. W. Gregory Sawyer for his help and guidance throughout this undertaking; without him, this dissertation would never have been realized. I would also like to thank my friends and family for their input, encouragement and comic relief. Finally, I thank my wife Melissa. Her support, above all others, has allowed me to achieve this goal in my life.

TABLE OF CONTENTS

	<u>page</u>
ACKNOWLEDGMENTS	4
LIST OF TABLES	7
LIST OF FIGURES	8
ABSTRACT	11
CHAPTER	
1 INTRODUCTION	13
1.1 Motivation of Research.....	13
1.2 Literature Review	14
2 EQUIPMENT DESIGN	20
2.1 Design Philosophy	20
2.2 High Vacuum Chamber	21
2.3 High Vacuum Pin-On-Disk Tribometer	23
2.4 High Vacuum Linear Reciprocator.....	27
2.5 Cryogenic Pin-On-Disk Tribometer	30
2.6 In Situ Wear Tribometer.....	33
2.7 Cryogenic High Vacuum Bushing Tribometer.....	36
3 VARIABLE ENVIRONMENT EXPERIMENTS	44
3.1 Overview of Materials Used in Experiments.....	44
3.2 Cryogenic Pin-On-Disk Experiment.....	45
Environmental Protocols	45
Experimental Procedure	47
3.3 <i>In Situ</i> Wear Experiment	49
Sample Description	50
Environmental Protocols	51
Experimental Procedure	52
3.4 Cryogenic High Vacuum Bushing Experiment.....	55
Environmental Protocols	55
Material Preparation	56
Experimental Procedure	56
4 RESULTS	58
4.1 Cryogenic Pin-On-Disk Experiment.....	58
Determining a Friction Coefficient	58

Experimental Results.....	58
4.2 <i>In Situ</i> Wear Experiment	64
4.3 Cryogenic High Vacuum Bushing Experiment.....	68
Preliminary Experiment.....	68
Solid Lubricant Coating Results.....	69
5 DISCUSSION.....	71
6 CONCLUSIONS.....	79
7 FUTURE DIRECTIONS	80
APPENDIX	
A UNCERTAINTY ANALYSIS OF FALEX POD TRIBOMETER.....	82
B HIGH VACUUM PIN-ON-DISK EXPERIMENT.....	85
Environmental Protocols	85
Experimental Procedure	85
Humid Air and High Vacuum Testing	86
Pump and Purge Test Results	86
C AUGER ELECTRON SPECTROSCOPY OF COATINGS	88
D GIBBS FREE ENERGY CALCULATIONS	91
LIST OF REFERENCES.....	94
BIOGRAPHICAL SKETCH	98

LIST OF TABLES

<u>Table</u>	<u>page</u>
3-1 List of coatings initially tested for environmental sensitivity	44
4-1 All the steady state wear testing in humid air and dry nitrogen.	68
5-1 Activation energy values from Monte Carlo simulations of all the data along with the uncertainties in those values.	75
B-1 Summary of results from high vacuum pin-on-disk tribometer in humid laboratory air and high vacuum. All tests were run at a normal load of 5N and a sliding speed of 20 mm/sec.	86
D-1 List of values for enthalpy and entropy for species in (D-1).(55)	91

LIST OF FIGURES

<u>Figure</u>	<u>page</u>
2-1 Vacuum chamber pump down curve with inset of residual gas analysis results at high vacuum.....	23
2-2 Pin-on-disk design variations	25
2-3 Components of the high vacuum linear reciprocating tribometer.....	29
2-4 Schematic of modified pin-on-disk tribometer used in the temperature studies. The forces in the system are depicted in the image above using grey arrows.	31
2-5 Cryogenic pin-on-disk sample housing.....	32
2-6 Overview of in situ tribometer.....	34
2-7 Bushing tribometer	37
2-8 Illustration of load path to ground for bushing tribometer design.....	39
2-9 Friction coefficient derivation for bushing tribometer results.....	42
3-1 Description of impinging jet technique used to cool and clean the surface of the disk during experiments.....	47
3-2 Screenshot of LabView software written for the in situ wear experiments.....	53
4-1 Friction plot of the electroless nickel coating at -25°C. The plot indicates the large fluctuations in friction coefficient throughout the experiment. The average value for this data was $\mu = 0.8$ with a standard deviation of 0.1. The temperature of the system is also plotted to indicate the small fluctuations in temperature over a 15 minute period.	59
4-2 Friction response of metallic coatings to varying temperature. The friction forces were scattered due to the large amount of surface deformation and wear that occurred during the test.....	60
4-3 Friction response of metallic coatings with solid lubricant impregnated. (a) The friction results for hard anodize with PTFE coating at -30°C. (b) The friction results for the metallic coatings impregnated with PTFE were much more uniform than the metallic coatings alone, but the coatings did not appear to be sensitive to changing temperatures.....	61
4-4 Results for bulk polymeric samples against a stainless steel pin. The PTFE-based samples displayed a linear decrease in friction coefficient with increasing	

temperature, while the UHMWPE sample maintained a constant friction coefficient regardless of temperature.....	62
4-5 Friction coefficients of MoS ₂ based solid lubricant coatings at varying temperatures. The nearly pure MoS ₂ with nickel coating (95% MoS ₂ , 5% Ni) had the lowest sensitivity to temperature. The commercially available MoS ₂ with Sb ₂ O ₃ and gold had the lowest recorded friction at 180°C and the highest increase in friction as temperature decreased (over an order of magnitude).	63
4-6 Methodology for calculating wear volume. (a) Plot of a line scan taken from the undeformed surface scan made by the Zygo prior to beginning the experiment and a line scan taken from the surface scan made after 6,000 cycles. (b) Estimation of the wear scar cross-sectional area using the difference between the two line scans. This area is multiplied by the length of the track to estimate a wear volume.....	65
4-7 Plot of volume lost vs. work input into the system. The plot indicates the wear of this coating is sensitive to the partial pressure of water in the environment. In this case, the wear rate initially in air is much less severe than transitioning from a dry environment to a humid one.	66
4-8 Plot of volume lost vs. work for the MoS ₂ with Sb ₂ O ₃ and gold coating. The uncertainty in this value is nearly 100% of the value due to the small volume loss over the course of the entire 2,000 cycles. This result led to testing at higher normal loads and larger numbers of cycles.	67
4-9 Initial experiment using fluorinated grease in a high vacuum cryogenic friction experiment.....	69
4-10 Plot of the friction response for all three coatings tested in the experiment. None of the coatings demonstrated an increase in friction with decreasing temperature in this geometry. The highlighted outlier in the MoS ₂ with titanium data set was the last data point and could indicate the onset of failure for the coating. Many of these coatings failed after only a few hundred to one-thousand cycles.	70
5-1 Illustration of a potential energy barrier typically found in activated chemical processes. The image to the left of the energy curve is a representation of Boltzmann energy distribution for a large number of atoms or molecules in a system at different temperatures. The portion highlighted in black is the area of the curve containing atoms with energies high enough to overcome the potential energy barrier.	72
5-2 Illustration of methodology for creating a Monte Carlo simulation of activation energies.	73
5-3 One data series in standard and logarithmic plot with fit.	74
5-4 Activation energy fits for all the MoS ₂ -based composite coatings. This value can be thought of as a thermal sensitivity for the coating.....	74

5-5 Plot of activation energies determined from the cryogenic testing of all the MoS ₂ coatings as a function of wear rate determined by the in situ experiments for the same coatings.....	76
5-6 The deck of cards illustration for sliding between lamellar MoS ₂ sheets. The interfaces that are shearing change throughout the sliding event, but the shear force does not change.....	77
A-1 Free body diagram of Falex pin-on-disk tribometer with friction coefficient calculations.....	82
B-1 Pump and purge data results for a thin coating and bulk polymer.....	87
C-1 Relative intensities for several elements plotted vs. position across the wear track for the MoS ₂ with titanium coating run in humid air environment. Auger data indicates a high content of titanium and oxygen (likely titania) on the surface inside the wear track. The signature of the other elements was relatively constant inside and outside the track.....	88
C-2 Relative intensities for several elements plotted vs. position across the wear track for the MoS ₂ with titanium coating run in dry nitrogen. Like the humid air data, dry nitrogen data indicates a higher content of titanium and oxygen (likely titania) on the surface inside the wear track. However, there are also distinct changes in the sulphur and molybdenum signatures inside the track indicating more MoS ₂ is on the surface.....	89
C-3 Relative intensities for several elements plotted vs. position across the wear track for the AFRL chameleon coating run in humid air. There is no signal from the molybdenum in this coating. Oxygen and carbon are primarily found inside the wear track while sulphur and antimony are depleted inside the track.....	89
C-4 Relative intensities for several elements plotted vs. position across the wear track for the AFRL chameleon coating run in dry nitrogen. The molybdenum, sulphur and carbon intensities increase inside the wear track. The difference between this scan and the open air tests indicate MoS ₂ is, in fact, drawn to the surface of the coating during wear.....	90

Abstract of Dissertation Presented to the Graduate School
of the University of Florida in Partial Fulfillment of the
Requirements for the Degree of Doctor of Philosophy

EVALUATION OF TRIBOLOGICAL RESPONSE OF MOLYBDENUM DISULPHIDE-
BASED COATINGS TO VARYING ENVIRONMENTS

By

Matthew A. Hamilton

August 2007

Chair: W. Gregory Sawyer
Major: Mechanical Engineering

Molybdenum disulphide-based coatings are the standard solid lubricant coatings for mechanisms intended to operate in low earth orbit. These coatings are known to provide low friction in a high-vacuum environment. In my study, a variety of hard metallic and solid lubricant coatings were tested in a self-mated configuration at temperatures ranging from -80°C to 180°C to evaluate the friction response to varying temperature. The tests were performed using a pin-on-disk tribometer inside an environment chamber at fixed normal load and sliding velocity. Systems where the contact was dominated by plastic deformation and wear debris generation showed no evidence of thermal sensitivity and had friction coefficients ranging from 0.2 to 0.9. However systems where motion was accommodated by interfacial sliding experienced as high as an order of magnitude increase in friction coefficient (0.02 to 0.2) as the temperature of the system was decreased from 180°C to -80°C .

The low friction coefficients of many solid lubricant coatings have been attributed to interfacial sliding in the material. In these experiments, the goal was to prove the systems were interfacially sliding by analyzing the evolution of surface topography. The results indicated that for the MoS_2 -based coatings it took an average of 30 cycles to remove a single atomic layer of MoS_2 (6 angstroms). This showed that interfacial sliding was occurring in a majority of the contact.

The end goal of the study was to comment on the application specific performance of the coatings in a bushing-shaft configuration. In this system, the friction coefficient showed athermal behavior caused by severe wear in the contact area. Ultimately designers of space mechanisms will have to determine the severity of the tribological contact in order to estimate the fluctuations in friction coefficient that may be experienced by varying temperature.

CHAPTER 1 INTRODUCTION

1.1 Motivation of Research

Designing mechanisms to perform in low earth orbit requires predictable performance from the sliding interfaces. There are several challenges facing designers of space mechanisms. First, the temperatures that may be experienced in orbit vary widely (-200°C to 200°C). Second, the pressures found in low earth orbit are below the limit for many traditional lubricants (1×10^{-9} Torr). Finally, the mechanisms are typically tested on earth prior to launch, so materials chosen must not only function in both environments but also resist oxidation and degradation due to ambient species. Any one of these variables can have an effect on the tribology of a sliding interface. Characterizing these effects and providing models for predicting performance under these conditions is the focus of this research.

Many designers characterize frictional losses in a system as a function of the mechanics of the system. While the mechanics can drive some of these losses, the environment can play an equally important role in the response of the system. The influence of temperature on the friction of a system can be dramatic. Polytetrafluoroethylene (PTFE) is a primary example of a commonly used solid lubricant that is affected by temperature changes. In this polymer, temperature changes can influence both its mechanical and tribological properties.(1-4)

Molybdenum disulphide (MoS_2) has become a standard solid lubricant for high vacuum or dry conditions. The interest in the tribology of MoS_2 can be seen in the large number of publications focused on this topic. There are however, two areas that have not been exhaustively studied. The first is the macroscopic friction response of MoS_2 coatings to decreasing temperatures. The second is an *in situ* quantification of wear for MoS_2 and MoS_2 -based composite coatings while cycling environment. A review of current literature yields only one

publication using MoS₂ in a cryogenic environment, but this paper was simply a publication of test results and offered no hypothesis for the results found.(5) A paper by McCook *et al.* looked at PTFE coatings at reduced temperatures and posed the hypothesis that friction of self-mated PTFE may be thermally activated. The group also notes the appearance of a cutoff temperature below which the friction no longer rises, but levels out.(6) A more recent work on highly oriented pyrolytic graphite (HOPG) also noted this type of thermally activated friction response including a temperature limit, however, this work was on a much smaller scale in ultra-high vacuum.(7) Another study performed by Schirmeisen *et al.* found this type of increasing friction for untreated silicon (111) sliding against a silicon tip.(7, 8) Like the experiment by Zhao *et al.* this experiment was performed at ultra-high vacuum (UHV) using an atomic force microscope (AFM). The results indicate there may be a physical limit where interfacial sliding of these materials is no longer the most convenient path for energy dissipation. However, it may be just as possible that the cutoff in each case is caused by separate phenomena. Therefore, the goal of this study was to determine if interfacial sliding of self-mated materials displayed a thermally activated behavior and to identify the transition from this behavior to athermal response at the macroscale.

1.2 Literature Review

Brief History of Molybdenum Disulphide Coatings

As early as 1941 there is reference to the low friction of ‘molybdenite’ in vacuum. It was discovered in a search for a replacement lubricant for the rotating anode x-ray tube.(9) One of the first substantial studies of MoS₂ as a solid lubricant was performed by Johnson, Godfrey and Bisson in 1948. They looked at the effects of contact pressure and sliding speed on the friction coefficient for a thin MoS₂ coating on steel in air. One conclusion drawn from the study was MoS₂ *‘is very effective in reducing friction at high sliding velocities. This film material was very*

tenacious, was chemically and thermally stable and consequently should have many practical applications.'(10) After the evaluation of the steady-state tribological properties in air, the sensitivity of friction coefficient of MoS₂ to buildup of surface oxide layers and crystallite orientation was reported by Johnson and Vaughn in 1956. This study held MoS₂ pins stationary for varying periods of time and observed the starting friction coefficient and steady-state friction coefficient. They determined that the 'buildup effect' caused an increase in the friction coefficient for a short time (less than 10 minutes) before it returned to a steady-state value. Once the system had run to steady state in one direction, the motor spindle was reversed to analyze the effect of crystalline orientation on friction. It was determined that orientation had no effect on steady-state friction.(11) The popularity of the new material led to expansion of its testing. Deacon and Goodman examined the role of elevated temperature on the friction of MoS₂ and several other lamellar solids. A pin-on-disk style of tribometer was used to measure the friction of a ¼" diameter hemisphere of platinum sliding on a flat disk of platinum both surfaces covered with a thin MoS₂ layer. The flat disk was heated from room temperature up to 600°C and friction coefficient was initially above 0.2 but quickly ran down to a value of 0.07 for temperatures from 40°C to 300°C at which point it steadily rose to a value of 0.5 at 530°C. The results indicated MoS₂ could maintain a friction coefficient less than 0.1 up to 300°C where the molecule began to oxidize to MoO₃ in air.(12) Because of the distinct difference in the friction of MoS₂ in air compared with high-vacuum Haltner and Oliver looked at the effects of the partial pressure of water on the friction response of MoS₂. Pellets of MoS₂ were run against a copper substrate to create a transfer film in air and friction response was observed while varying the humidity surrounding the sample from ambient levels 25% RH to 0.5% RH. This study posed a model for friction coefficients as a function of increasing partial pressure of H₂O in the

system.(13) Further environmental studies were done with MoS₂ in ultra-high vacuum ($p < 10^{-9}$ Torr) where the temperature was elevated to over 930°C before thermal decomposition was reached.(14) Ross and Sussman found the oxidation of MoS₂ to MoO₃ to be a self-limiting process; meaning the formation of a monolayer of oxide prevented further oxidation. The study showed steep initial increase in the percentage of MoO₃ when exposed to humid air, but as the exposure time increased, there was no increase in MoO₃.(15)

After the discovery of the low friction and thermal stability of MoS₂ films it became a primary candidate for many aerospace applications, particularly elevated temperature systems such as jet engines. A study of the friction of the available MoS₂ coatings at temperatures ranging from -75°C to 200°C was published by Hopkins and Campbell in 1969. A majority of the coatings in this experiment were MoS₂ with graphite using different binders (epoxy, sodium silicate, etc.). The focus of the study was to determine how different binder materials affected the friction and wear performance of MoS₂ films. The coatings were applied using an air brush then cured onto the surface. The data from these tests indicated a trend of decreasing kinetic friction with increasing temperature.(5) Other studies focused on the wear life of burnished coatings in an effort to improve the life expectancy of the coating.(16) Up to this point, a majority of the studies used manual deposition such as burnishing, painting or evaporating the material onto the sample. A number of groups were also working on improving deposition techniques for MoS₂. The performance of sputtered MoS₂ films was first studied by Talivaldis Spalvins. His studies showed an increased wear life and a more stable friction response over the life of the sample for a sputtered MoS₂ films in vacuum on a variety of substrates.(17, 18) One important conclusion that appeared in most of the papers on deposited films was cleanliness of the substrate heavily influenced the performance of the film. Another discovery, documented by

Petrov *et al.*, was the effect of the substrate temperature deposition on the degree of crystallization and the evolution of the structure inside the film during growth.(19) The study by Holinski and Gansheimer on the lubricating mechanism of MoS₂ indicated the layered structure shears easily and covers rough asperities on the surface. The interactions between MoS₂ layers are weak allowing for low shear strength and low friction coefficient. This study illustrates the sliding as a deck of cards where multiple layers participate in the shearing events simultaneously. Using SEM, the authors were able to quantify that roughly 25 atomic layers participated in sliding during the bearings tests performed.(20) Finally, the crystallinity of the MoS₂ coating was interrogated. This study indicated that an amorphous MoS₂ had poor tribological properties, in particular a high friction coefficient ($\mu = 0.4$) and acted as an abrasive that wore the counterface. Spalvins also studied the wear process for MoS₂ films that grew in finger-like structures from the substrate. The results indicated that these structures break early in the wear process leaving a well-adhered thin layer of MoS₂ bonded to the surface to accommodate the shear.(21)

The success of new deposition techniques (e.g. radio frequency (RF) magnetron sputtering(22), DC-diode sputtering(23) and RF diode sputtering(24)) gave researchers the ability to form composite coatings and study the effects of other constituents added to the MoS₂ films. Initially the hope was to reinforce the MoS₂ and extend its life, but as new materials were introduced and deposition techniques were improved another goal arose; to combine other materials with MoS₂ that could help prevent oxidation of MoS₂ and provide solid lubrication for environments where MoS₂ was not the best choice (namely humid air). This goal has remained a focus for many groups developing high performance solid lubricant films over the past 30 years. Zabinski *et al.* studied the morphological and tribological properties of MoS₂ films codeposited

with a variety of materials to identify changes that accompanied improved friction and wear characteristics. In this study, gold, iron, nickel and antimony trioxide were used as dopants for MoS₂ films. They concluded a decrease in crystalline grain size decreased the friction coefficient and improved wear resistance of the coatings. In the study a composite of MoS₂/Sb₂O₃/Au resulted in the smallest grain sizes of all the coatings.(25) Further studies under increased temperatures led to the development of a yttria-stabilized zirconia (YSZ), gold, MoS₂, diamond-like carbon (DLC) composite termed a ‘chameleon’ coating. This coating was developed at the Air Force Research Labs (AFRL) and produced a friction coefficient of 0.10 in air reportedly due to the graphitic carbon from DLC and 0.02 in a dry nitrogen environment because of MoS₂. As the temperature of the system was elevated to 500°C, sliding was accommodated by drawing gold to the surface yielding a friction coefficient of 0.15.(26) Many other studies have been performed using MoS₂ in combination with other constituents in an attempt to further improve performance over an increasing range of operating temperatures and environments.(27-31)

Other developments in coating technologies are the use of composites to control the nanocrystalline structure of the coatings. The AFRL has performed a number of studies on the structure of coatings using different recipes and correlated that with tribological performance of the films.(26, 32-34) Another improvement in thin film coatings is customizing the surface prior to applying the coatings. By designing the surface topography, it is possible to control how the surface will wear and ensure that the contact is never starved of lubricant. One technique that has gained popularity is texturing the surface prior to applying coatings. Using a laser, micron-sized dimples are created on the surface of a solid created. These holes act as reservoirs for the solid lubricant so it is replenished as the surface wears. This technique, developed by Andre

Voevodin at AFRL, has had success at maintaining low friction for extended numbers of cycles.(35)

Although the use of deposition techniques has added diversity to the materials chosen to be added with MoS₂ for new coatings, it has also been shown to negatively influence the quality of the MoS₂. Several studies have been performed on testing the quality of MoS₂ in deposited coatings and found that the background pressure of the deposition chamber drastically affects the ratio of Sulphur to Molybdenum in the coatings. For deposited coatings where the chamber pressure is on the order of 1×10^{-4} to 1×10^{-3} Torr, the ratio for S to Mo in the resulting coatings ranges from 1.5 to 1.9. These coatings demonstrated a range of friction coefficient values from 0.007 to 0.1 in inert environments.(36) However, in systems where deposition occurs under ultra-high vacuum (1×10^{-9} Torr or less) the ratio is 1.97.(37) The very pure MoS₂ coatings had recorded friction values below 0.002 in vacuum.(36) The poor quality of the sputtered MoS₂ leads to Oxygen substitution in the lattice structure and edge sites throughout the coating that are primary nucleation points for oxidation to MoO₃.(38)

CHAPTER 2 EQUIPMENT DESIGN

2.1 Design Philosophy

The goal in the design of the high vacuum tribometers was to create devices that functioned inside a vacuum chamber, but required no chamber in particular. In other words, the tribometers could not require mechanical feedthroughs. There were two reasons driving this decision initially. The first was that only one vacuum chamber was being fabricated, and to keep that chamber as simple as possible, no mechanical feedthroughs could be required. The second was that keeping the motor for the system inside the chamber as near to the sample as possible minimizing immeasurable losses that arise when complex loading and motion systems are used to accommodate these feedthroughs. Driving the systems with vacuum compatible motors simplified the designs guaranteeing that all loads reacted by the sample are read by the load cell in each system. This design decision requires a motor and stage system that can reliably oscillate for millions of cycles without adjustment. All the other components can be adjusted prior to evacuating the chamber; however, a motor failure ruins the experiment.

The philosophy of connecting a load cell directly in the path between the sample and ground was put forth by Schmitz et al. as one that minimizes the uncertainties in the force measurements.(39, 40) This philosophy is followed in all the custom-built tribometers discussed here. To maximize the sensitivity of this tribometer, the load cell is mounted so the friction force is measured by the most sensitive axes of the load cell. In some cases, the load cell is oriented so the normal force is also measured using the more sensitive axes, particularly in cases where the designed normal load is small compared to the capacity of the load cell.

During the construction of the tribometers, the software written for each one was equipped with the ability to record phase-locked data. This means the positional data is recorded

simultaneously with normal load and friction force. This data is useful for debugging issues with the design and can expose structure in the data that is caused by synchronous topography in the sample.

2.2 High Vacuum Chamber

The ambient pressures at 20 km and 2,000 km are 10 Torr and 1×10^{-15} Torr, respectively. In a vacuum system, pressures above 1×10^{-3} Torr can be maintained through a controlled leaking of gas into the system. Ultra-high vacuum levels ($< 10^{-9}$ Torr) are typically obtained through metal sealed stainless steel chambers that are baked to remove water and continuously pumped. A decision to operate at high vacuum levels ($< 10^{-6}$ Torr) was made in effort to minimize complexity and maximize sample throughput. Because of gas surface interactions (41) that can often cause dramatic changes in the frictional behavior, the vacuum level or level of cover gas cleanliness required to simulate space environments continues to be discussed and is likely a function of sample material, geometry, and sliding speed (some authors suggest that pressures as low as 10^{-3} Torr may be sufficient for certain materials (32, 42)).

Controlling the environment around the tribometer is the most critical aspect of vacuum tribology equipment. For this tribometer a custom-built stainless steel vacuum chamber was designed to reach the base pressure of 1×10^{-6} Torr in less than two hours. The transition from viscous flow to molecular flow (occurring $\sim 1 \times 10^{-3}$ Torr) requires a pump for each regime. A dry-scroll pump was selected for the viscous flow regime (low vacuum) because of its high pumping speed and its oil free operation, which ensures there can be no back streaming of oil that would contaminate the chamber.(43) A cryogenic vacuum pump is used after the crossover to the molecular flow regime (high-vacuum). This system works using a liquid helium compressor to cool a series of surfaces inside the pump from 77 K to 4 K. The fundamental theory behind cryogenic vacuum pumps is that desorption of chemisorbed and physisorbed molecules on a

surface is exponentially dependent on temperature(44). There are a number of reasons that this type of high vacuum pump was selected. First with a turbomolecular pump the system can be destroyed by a sudden increase in pressure. These pressure rises could be caused by a leak or a valve being opened mistakenly. The increase in pressure on one side of the system of turbine blades causes them to deflect enough that they will collide with the second level of blades resulting in catastrophic failure. However, if this occurs in a cryogenic pump, the pump will be saturated and can no longer pump gases. The solution to this is to empty or regenerate the pump by allowing it to warm to room temperature again. The second reason is the pump system works using cryogenic stages so water is pumped at a much higher rate than with a turbomolecular pump. Although the pumping speeds for air and nitrogen are equivalent between similarly sized cryogenic and turbomolecular pumps (1500 L/sec), the pumping speed for water is 266% higher for the cryogenic pump (4000 L/sec) than it is for the turbo pump (1500 L/sec). In stainless steel vacuum chambers, water is often the primary source of background pressure for the system. The pump-down curve for the vacuum system is plotted in Figure 2-1, along with the species found in the chamber as reported by the residual gas analyzer. Clearly the partial pressure of water is still the largest contributor of all the species found at this pressure. In an effort to drive as much adsorbed water as possible from the interior surfaces, heater jackets were wrapped around the external surface of the vacuum chamber; this helps to help to drive water off the surface during pump-down and helps to reduce the rate of water adsorption when the chamber is vented. The background pressure is read by a pressure gauge mounted directly to the chamber, which outputs a 0V to 10V signal indicating the pressure reading. The system can also determine ambient species present inside the chamber by using a residual gas analyzer (RGA). The RGA works by ionizing a sample of the molecules present in the chamber and measuring their mass to charge

ratio. This ratio is often unique to a single molecule or group of molecules and offers insight into the molecules present due to the environment and those coming from the sample itself.

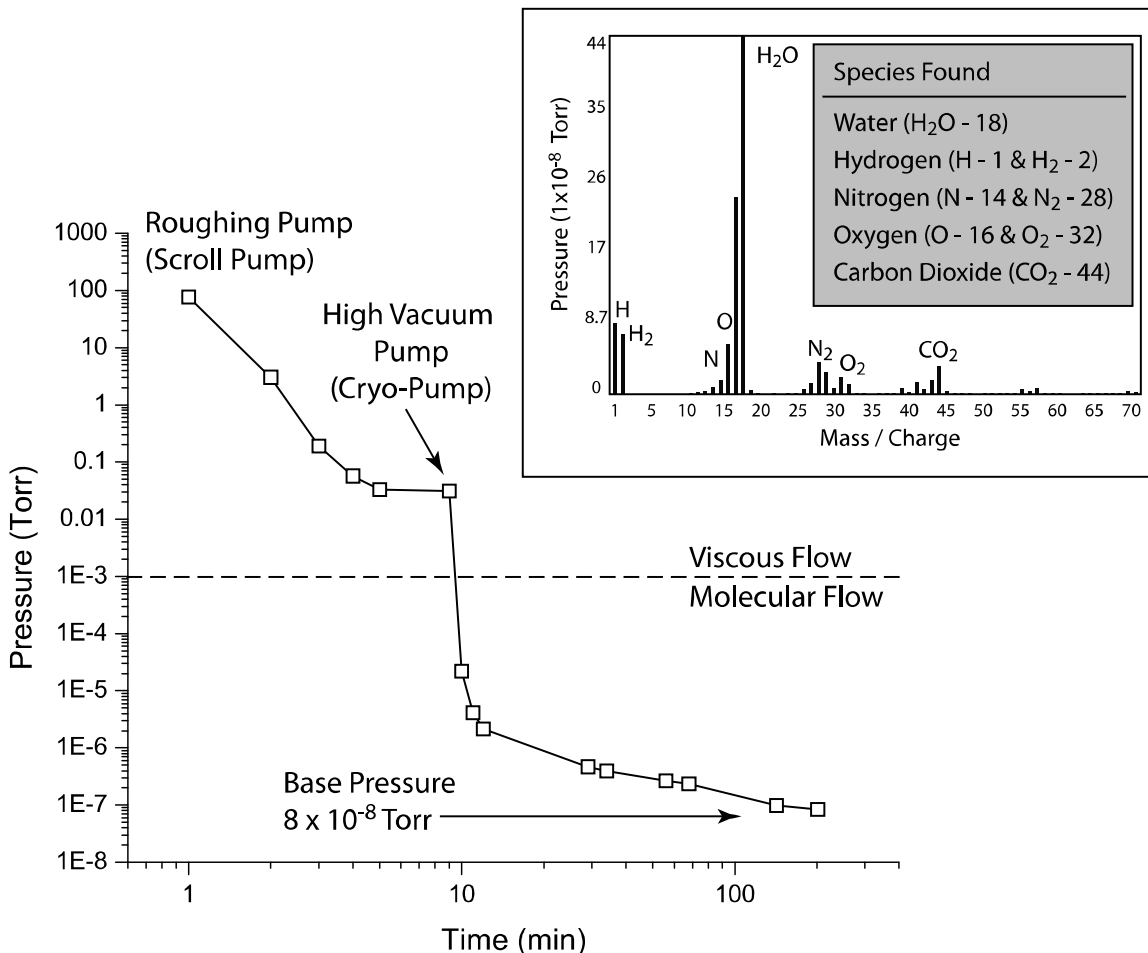


Figure 2-1 Vacuum chamber pump down curve with inset of residual gas analysis results at high vacuum.

2.3 High Vacuum Pin-On-Disk Tribometer

Mimicking a space environment inside the laboratory presents multiple challenges, one of the most debated issues is the vacuum level required to accurately reproduce space performance. There is no industry standard for this value, but the Harris Corporation indicated that a vacuum level of 10^{-6} Torr is suitable for performance testing of mechanisms. With this in mind, a pin-on-disk tribometer was designed and constructed that would be capable of operating in this pressure

regime. Many of the friction studies performed on solid lubricant coatings are run using pin-on-disk tribometers. There are several advantages for this type of tribometer. The disk is only expected to run in one direction meaning a simple motor can be used. The friction forces are only measured in one direction so it simplifies the load sensing requirements, and these systems can typically generate large numbers of cycles in a short period of time. This can be beneficial when trying to run a low-wear film to failure.

As mentioned each tribometer is driven by a high vacuum compatible motor capable of operating at pressures below 10^{-6} Torr. The motor that was chosen was a T-Max 5 servo motor from Nutec Components Inc. (www.nutec1.com). The unit is a motor and stage combined into a single housing. The drive is from a linear motor that has been wrapped around a central axis giving it the ability to turn the stage. This motor is capable of generating 2.9 N-m of torque continuously. This value is much higher than any torque expected from a pin-on-disk type contact under loads of 1 to 10 N. The spindle can be commanded to spin at speeds ranging from 0.001 rpm to 1,000 rpm allowing for a wide range of operating speeds. Nutec also outfits all its motors with positional encoders so the controller can determine the current position at all times. The encoder built into this system has 72,000 lines resulting in a resolution of 18 arc-seconds.

The load cell for this tribometer is an AMTI (www.amtiweb.com) MC-2.5A six-axis transducer. The choice to use this load cell was based on availability. At this time no other manufacturer could guarantee vacuum compatibility to the required levels. The transducer was modified to ensure vacuum compatibility below 10^{-7} Torr. The main changes are removing any paint and decals from the device and replacing all the wiring inside with Teflon coated copper wires to reduce outgassing. This load cell has a maximum capacity of 450 N in the axial

direction and 225 N in the radial directions. The resolution of the load cell in these directions is 15 mN meaning the lowest resolvable friction reading under a 1 N normal load is 0.015.

To manipulate the sample, the entire assembly is mounted to a set of Schneeberger (www.schneeberger.com) micrometer stages. The purpose of these stages is to accurately adjust the track diameter to fix the sliding speed, and to load the sample against the surface after properly positioning the pin.

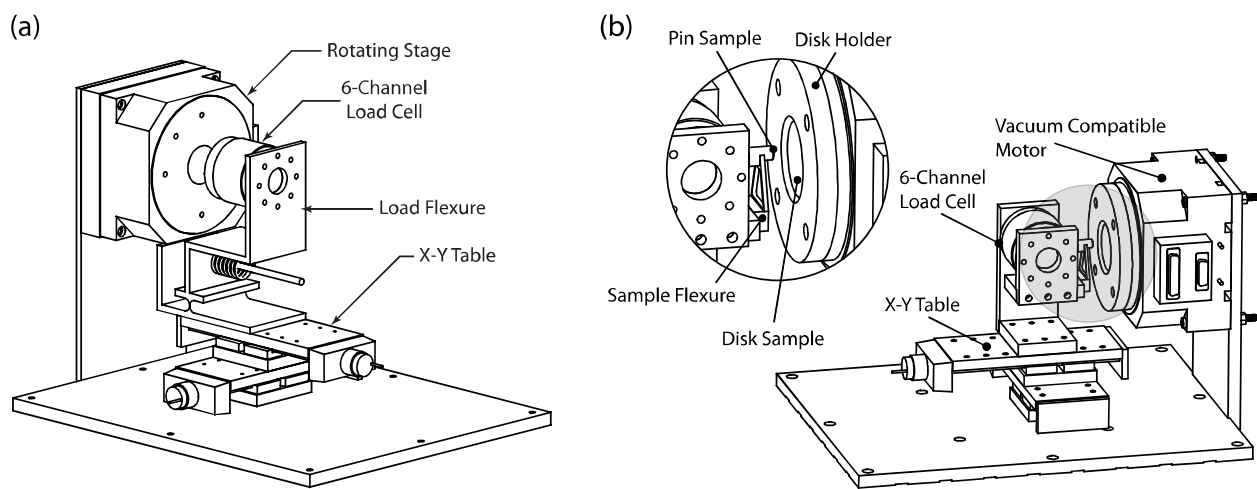


Figure 2-2 Pin-on-disk design variations (a) Initial pin-on-disk design used flexures and a compression spring to apply the load to the system. Also, note the orientation of the load cell. In this configuration its least sensitive axis is in the normal loading direction. (b) The final design uses a cantilevered pin holder to apply the load drastically increasing the stiffness of the system. The load cell is now mounted so the normal force and friction force are measured by the most sensitive axes of the transducer.

The machined parts in the pin-on-disk assembly went through a major revision. Initially, the device was loaded using a flexure and compression spring assembly (Figure 2-2a). After construction it was found that the dynamics of this system made it difficult to accurately measure friction, particularly if the surface had a misalignment. Any misalignment between the surface of the disk and the pin resulted in a sinusoidal fluctuation in normal force. The stiffness of the system was low enough that the vibrations induced by this forcing function caused the pin to

bounce off the disk surface. As a result, a new approach was taken in the revision where a cantilevered sample holder was designed and used to apply a load to the disk (Figure 3b). In the new design, the load cell orientation was altered so the two most sensitive axes were measuring normal load and friction force. The new revision simultaneously simplified the design, improved the sensitivity of the measurements and increased the stiffness of the system. While any misalignment between the motor and the pin still caused sinusoidal fluctuations in the normal load, the value was accurately measured and there was no evidence that the pin ever left the surface of the disk as it had with the first design.

The sample holders for this tribometer are capable of housing multiple disk sizes as well as multiple pin sizes. The modular disk housing has a base component that bolts to the face of the motor. A second component is screwed down over the disk pinching it against the base plate and aligns the disk face with the face of the motor. The housing can accommodate samples of varying thickness because of a compressible o-ring of Viton behind the sample that keeps it pressed to the alignment surface on the housing. The ball holder is machined into the load flexure for this tribometer. As with the disk holders, there are multiple flexures to accommodate different diameter pin samples. The sample is inserted into the holder and a set screw is tightened behind the ball holding it firmly in the housing and preventing it from slipping during the experiment.

The acquisition of data is done using a 6036E data acquisition card from National Instruments (www.ni.com). Each of the channels (normal force, friction force, ambient pressure and motor position) are recorded at up to 10 kHz (a value of 1 kHz was typically used). The length of time over which data is collected is variable to allow for different cycle times. A general guideline was to collect data for a minimum of two cycles to help reduce the effects of

noise in the data as well as any surface anomalies that may skew the result. This data is then averaged and appended to the average data file along with a timestamp. Phase-locked data is also available from this tribometer. This data is periodically collected and stored in a separate data file for further analysis.

2.4 High Vacuum Linear Reciprocator

A primary issue with pin-on-disk testing is contact pressure for this type of a sphere on flat geometry is very high. Usually the contact pressures are well above the yield strength of the coating materials. If a larger pin is used to reduce contact pressures, the sliding speed across the contact is varying as a function of radius. To counteract this effect, the wear tracks are usually narrow and can be difficult to analyze. Many microscopy techniques require the area of interest to be between 100 μm and several mm for an accurate sampling (e.g. x-ray photoelectron spectroscopy).

One alternative tribometer design is a linear reciprocator. This type of tribometer allows for a wide range of pin geometries. These pin geometries can greatly reduce the contact stresses on the films and allow a much larger wear track that is more easily analyzed in an XPS or other spectroscopy equipment. Adjusting the surface temperature of a sample on the linear reciprocator is also much easier than a pin-on-disk. The stage moves in a linear reciprocation over a fixed distance, so flexible cryogenic lines can be attached to the stage for adjusting the surface temperature. In a pin-on-disk contact, the disk sample is rotating and creating a viable conduction path for cooling the surface is not as straightforward.

The stage used in this design is a Lineax 10 from Nutec Inc. (<http://www.nutec1.com>). The motor and stage are capable of operating at high vacuum levels (pressure $< 10^{-6}$ Torr). The motor itself is a brushless linear motor and is equipped with a non-contacting encoder system. The maximum speed of the motor is 3m/sec with a positional resolution of 0.5 μm and a

repeatability of $2.5\mu\text{m}$. The stage is capable of handling a normal force of 1000 N and tangential force of 325 N. However, as the load is increased, so is the current required to drive the stage, resulting in larger amounts of heat generated due to resistive heating in the motor. A closed-circuit cooling system was embedded in the motor housing which can be hooked up to a chilled water system to maintain a safe operating temperature. This is in contrast to the pin-on-disk tribometer which does not require cooling due to the low forces and torques generated in those experiments. The maximum track length of 50 mm is defined by the motor travel. The mounting plate on the stage has an array of tapped 4-40 holes to allow for a variety of counterface positions.

The load cell used in this system is the same type as described earlier for the high vacuum pin-on-disk tribometer, a MC-2.5A from AMTI. The only difference is the load capacity and resolution of the load cell. This system is designed to work with loads as high as 1000 N, so a 2200 N load cell is used. With all of the load cells from AMTI (the MC-2.5A included) the resolution in the normal or z direction is twice that of the x and y directions. To enable small friction coefficients to be measured by this system the more sensitive x and y axes are used to sense the friction force. As mentioned, the resolution of these load cells is scaled based on their maximum capacity. The transducer used here cannot resolve a friction force less than 75 mN. However, the normal loads intended for the tribometer are between 100 and 1000 N resulting in a minimum resolvable friction coefficient of 0.001 at 100 N.

Due to the size of the linear stage, several loading options were precluded. Ultimately, the choice was made to use a cantilevered arm loaded with a compression spring, which can provide a variety of loads by varying the stiffness of the compression spring. The system works by using a t-shaped arm that pivots about a pair of bearings mounted to the frame of the tribometer. As

the spring is compressed, it imposes a force on the top of the t-shaped component in the horizontal direction. The body pivots about the bearing axis and imposes a vertical force on the stage to balance the moment. There is no mechanical advantage in this system; theoretically, the load applied by the spring is the same as the one applied to the stage. This was done to make it easier to estimate the required spring stiffness and compression for a desired load. One advantage of using a simple design is low number of components. Every moving part and surface interface in a vacuum system is a possible source of virtual leaks and outgassing. By minimizing the number of mating components, it is possible to improve pump down times and sample throughput.

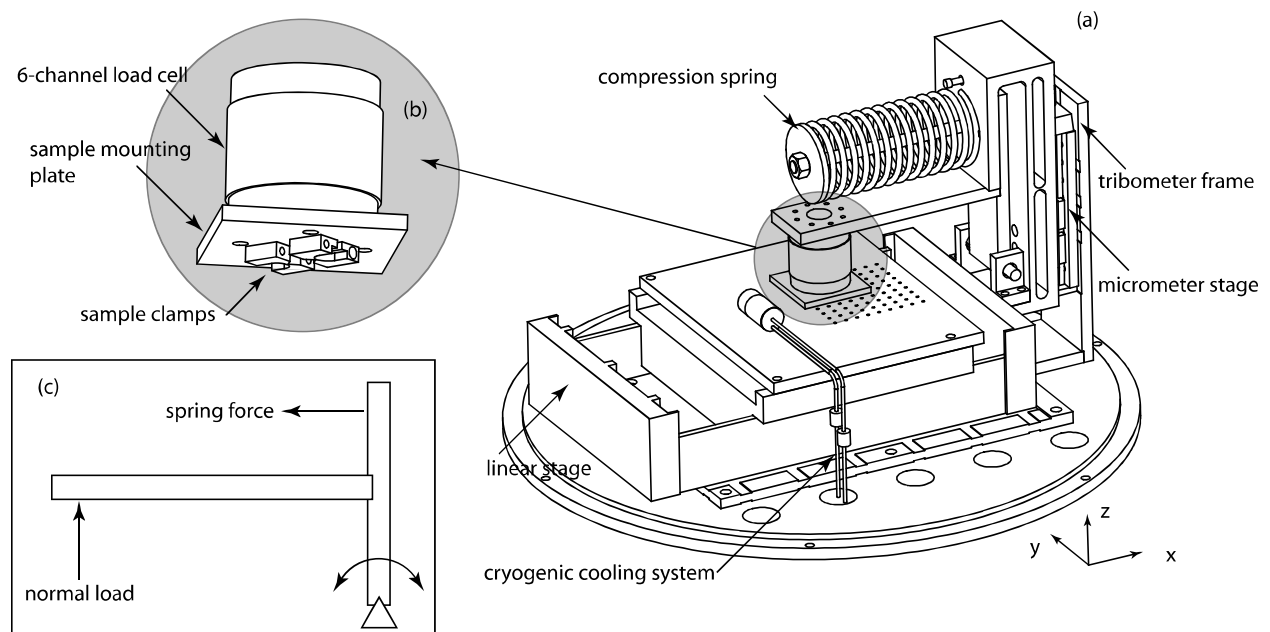


Figure 2-3 Components of the high vacuum linear reciprocating tribometer. (a) Schematic of the high vacuum linear tribometer. (b) Pin sample holder assembly. (c) The compression spring pulls the t-shaped lever arm forward imposing a normal force on the surface between the sample and the counterface.

Although the assembly works using a similar theory to the original pin-on-disk device, the dynamics of this system should not result in the same issues as the pin-on-disk. This is primarily

due to the higher spring stiffness and large normal loads applied to the surface. Another difference between the systems is the forcing functions. The pin-on-disk tribometer generates a sinusoidal forcing function with a frequency equal to the cycle frequency. The linear reciprocator does not generate the same type of forcing function. Any misalignment between the surface and the pin will manifest itself as a ramp with a frequency equal to the cycle frequency.

2.5 Cryogenic Pin-On-Disk Tribometer

At the core of the apparatus is a Falex Pin-On-Disk tribometer (see figure 2-5). This system uses a dead-weight load to apply a normal force onto a pin sample. The pin remains stationary while the disk below it spins. The shear force acting at the interface between the pin and disk results in a friction force on the pin. This force pulls the armature attached to the pin inducing a strain across the load cell connecting the armature to ground. The force is measured by the deflection of a strain gauge and fed into the internal electronics of the tribometer to calculate a friction coefficient. The user inputs the mass of the dead-weight load attached to the armature. The friction coefficient is calculated based on the ratio of the distance from the load cell to the gimbal and the pin sample to the gimbal. A more detailed discussion of the friction calculation and the uncertainty in the measurements from this tribometer can be found in Appendix A.

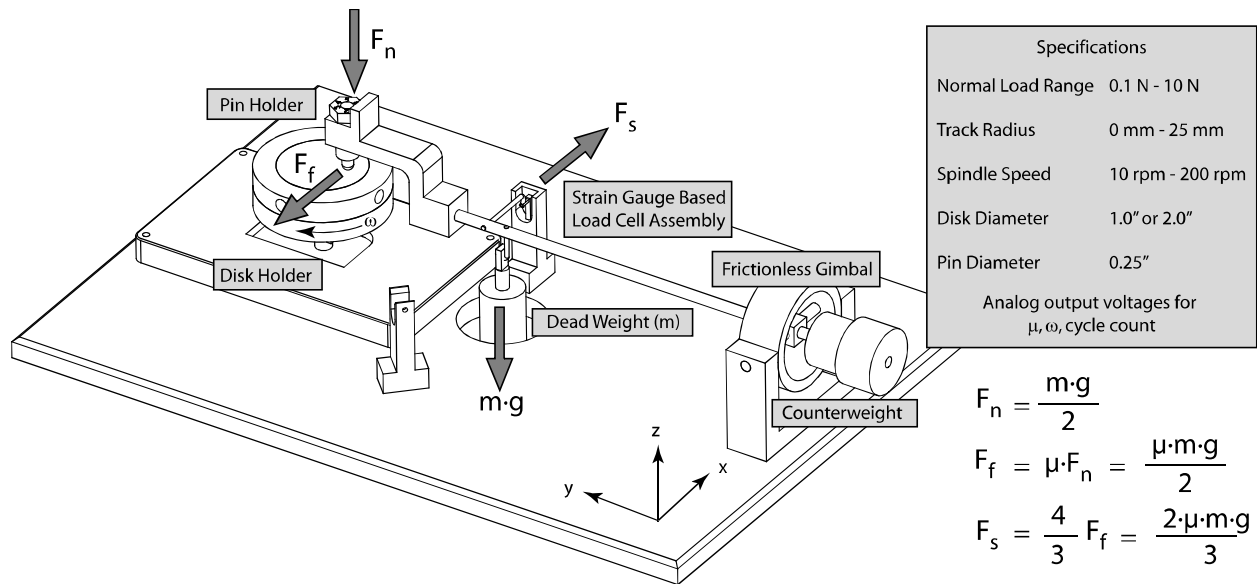


Figure 2-4 Schematic of modified pin-on-disk tribometer used in the temperature studies. The forces in the system are depicted in the image above using grey arrows.

There were two major changes from the as-received Falex system to better accommodate the testing. The first change was the disk holder. The second generation holder was created for easy sample changes. The housing itself is made up of two parts. The lower half is mounted to the spindle driven by the motor. This portion aligns based on the spindle shaft and is tightened onto the shaft using a clamping mechanism. The top portion is modular so that multiple sample sizes can be used. Currently, two sample sizes can be used. The first is a 2.0" diameter disk with a range of thicknesses from 1/8" to 5/16", which was used for all the testing described here. The second is a 1.0" diameter disk with the same thickness range. The lower half of the housing has a reverse-threaded stud coming out of the top. The upper half threads onto this stud and is tightened using a tool provided by Falex. The holes on the outside of the upper half are used by the tool to apply more torque for tightening the sample housing.

The second major change was the pin holder. The holder was similar to the original Falex holder in that it had a hexagonal head to allow multiple tracks to be run on a single ball. The

difference comes in how the ball is attached to the housing. The large temperature fluctuations in these experiments proved a problem for the original holder because the samples were glued to the housing. It was necessary to change the design and create a mechanical connection between the ball and housing. This was accomplished by using a threaded stud that runs down the center of the housing. The balls used must have a 4-40 threaded hold tapped in them, the stud has 4-40 threads on the lower half and left hand threaded 1/4-20 threads on the upper half. Once the ball is threaded onto the lower half, the stud is rotated back into the housing causing it to tighten the ball further and provide a strong force to keep the ball in place. Once the sample is mounted, decreasing the temperature causes the ball to be further pulled into the housing because the stud inside is made of aluminum while the housing is stainless steel.

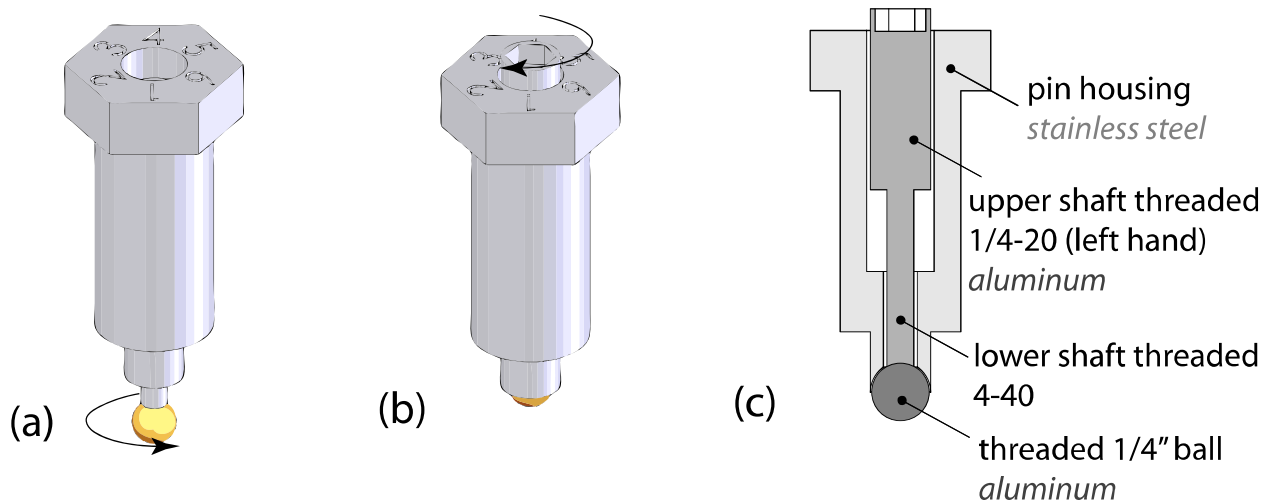


Figure 2-5 Cryogenic pin-on-disk sample housing. (a) Thread the ball onto the lower shaft using a standard counter-clockwise motion until it is tight. (b) Rotate the upper shaft in the clockwise direction to retract the ball into the housing. The ball will fit snugly into the mating surface inside the pin housing. (c) Section view of the assembly after the ball has been properly tightened. The materials for each component are also highlighted to indicate the system will further pull the ball into the housing as the temperature of the system is decreased.

2.6 In Situ Wear Tribometer

The ability to determine the life expectancy of a solid lubricant coating is of great importance to designers. Mechanisms must be designed to operate within a useful lifetime, but it is difficult to accurately predict that life without some guidance on how the system will fail. Solid lubricant coatings generally fail due to some type of wear mechanism be it delamination, abrasive wear, plowing etc. Characterizing the type of wear a solid lubricant coating experiences and its severity can improve designs where these materials are the limiting factor. To accomplish this, a tribometer was designed and constructed for the purpose of measuring wear of a surface in situ.

Wear track topography can vary widely based on geometry of the contact and composition of the surfaces. In the case of many solid lubricants, wear rates are between 1×10^{-4} and 1×10^{-8} mm^3/Nm . This means it could take several thousand cycles before a nanometer of the surface is removed. Given the sensitivity required to capture the surface evolution, the decision was made to use a scanning white light interferometer (SWLI). The Zygo New View 5030 was chosen because of the quality of its optics, and a feature height resolution on the order of angstroms. This system is equipped with set of motorized stages capable of adjusting the sample orientation (roll and pitch) and position (x, y, z) to provide the best surface scans. The difficulty was designing a tribometer capable of functioning in this limited workspace.

Like the vacuum tribometer, finding a motor and stage system suitable for the intended environment proved difficult. Initially, a small stage was chosen which was driven by a brushed DC servo motor. The motor was found to have problems running for extended periods in low humidity environments. This is most likely due to the graphite brushes, commonly found in many servo motors, becoming brittle in an environment that lacks moisture. The second version of the stage was a Parker 401-XR linear stage with a HV172 stepper motor. This system is

capable of sustaining a much larger load than the previous version (200 N compared to 5 N) and came with a linear encoder for monitoring stage position. Measuring absolute position of the stage provides better repeatability in the measurement that estimating the position using motor rotations. More specifically, the coupling between the motor and stage has dead zones that cannot be accounted for when the position is being estimated by motor revolutions. The stage and stepper motor combination have a positional repeatability of $\pm 5\mu\text{m}$. The repeatability is important when producing the time-lapse images of the track because any systematic drift of the stage is readily apparent in the resulting video. The new stage also expanded the range of possible sliding velocities with a maximum velocity of 50 mm/sec.

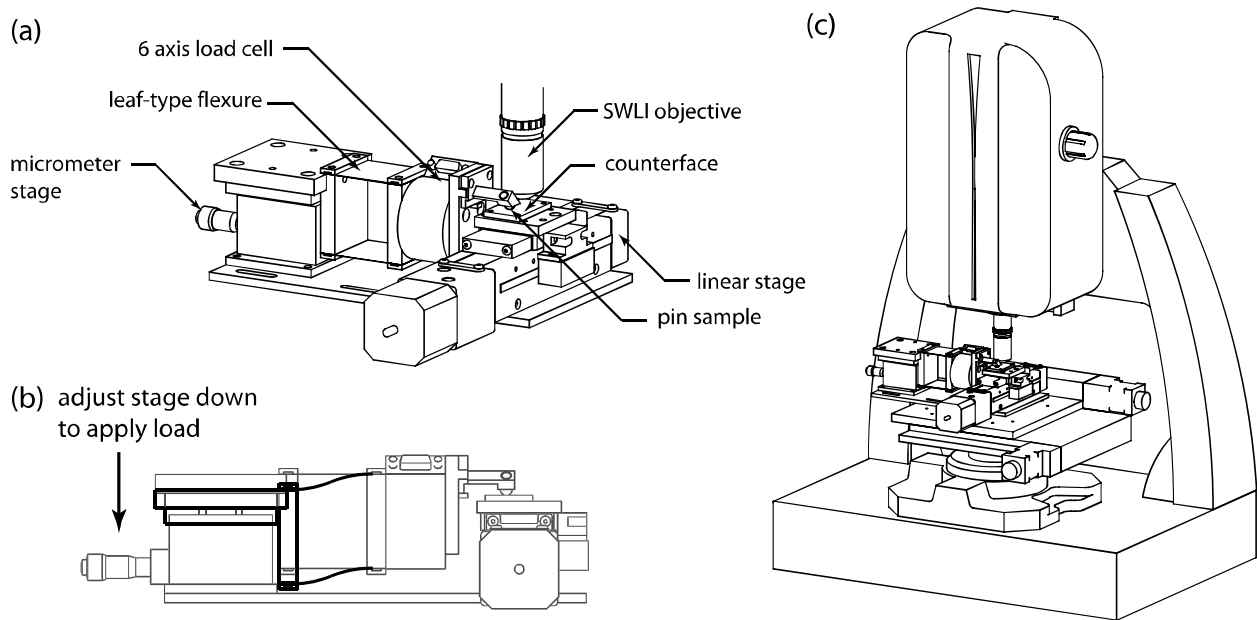


Figure 2-6 Overview of in situ tribometer. (a) Schematic of in situ tribometer. (b) Illustration of loading mechanism. (c) Drawing of tribometer placed on top of the Zygo stage.

The intended normal load for the tribometer was less than 10 N which required a load cell that could read friction forces as low as 50 mN. A JR3 50M31A load cell was chosen with a resolution of 28 mN in the normal load direction and 14 mN in the friction force direction.

Following the design philosophy mentioned earlier, the six-axis load cell was placed directly in the load path between the pin sample and ground. This is believed to be the best way to minimize uncertainties in the friction and normal force measurements.

The application of load in this tribometer had to be small to allow the system and a surrounding environment chamber to fit inside the framework of the SWLI. The size constraints on this tribometer limited the options for the load application mechanism. The design employs a leaf-type parallelogram flexure attached to a micrometer stage to apply a load to the pin sample. One benefit of this type of design is the wide variety of normal loads that it can apply by changing the geometry of the leaf flexures. A second property of this type of flexure system is its high stiffness in the friction force direction. This will help to prevent the system from rotating as the force between the pin and the counterface increases. By adjusting the micrometer stage, the pin sample is brought into contact with the counterface. The load increases as the deflection in the leaf flexures increases. The six-channel load cell is used to read the applied normal load in real-time to allow the user to accurately reset the load after the pin has been brought off the surface for imaging purposes.

The pin sample holder is a PEEK component machined to hold the ball at a 60° angle with the surface. The purpose for this is to maximize the number of tracks that can be run on a single ball. By angling the ball in this way, a single sphere may be used for up to 6 tests. This matches the number of tracks that can be run on the rectangular coupons. The counterface is mounted to a machined plate attached to the motorized stage. The hole-pattern on the plate is such that the counterface can be held in three different positions. Each position can have two tracks run on it for a total of six tracks per sample.

2.7 Cryogenic High Vacuum Bushing Tribometer

Solid lubricants and fluorinated greases are commonly used in bushing configurations to provide continuous operation in extreme environments where many traditional lubricants are unable to operate. Thermal limits (high and low) often preclude the use of many hydrocarbon oils. High vacuum environments are particularly challenging and there are a number of moving mechanical assemblies that utilize bushings to provide low torque operation in space and high altitude vehicles.

Bushing contacts are typically designed to be closely matched axis-symmetric bodies of revolution (shaft and through hole). Such a common and practical device, bushings are used in everything from door hinges to jet-engine actuators. Surprisingly, there is little published on component level testing of bushings; perhaps, due to the multitude of quiet complexities found in such simple and ubiquitous components. These complexities include evolving geometry during operation (45), and uncertainties in contact area, pressure distribution, and frictional forces. In an effort to study the extended performance of a single bushing component, a cold thermal vacuum bushing tribometer was constructed.

The design of the tribometer followed the methodology described by Schmitz et al.(39), which essentially describes the importance of having the load path flow through a 6-channel load-cell that reacts the normal and frictional forces and moments near the point of contact. A six-channel load cell suitable for high-vacuum operation was designed and fabricated by AMTI (Boston, Mass) and having a maximum load of 1000N in the loading direction and maximum of torque of 50Nm. The load cell is a strain-gauge based six-channel device used to sense the load that is transferred from the flexures into the contact between the bushing and the shaft. It measures the normal load applied to the bushing as well as the frictional torque generated at the

bushing-shaft interface. The forces and torques are output by the load cell electronics as analog voltages that can be recorded as the test is running.

Traditionally, dead weight loads, pneumatics, or hydraulics are selected to apply loads in tribological testing. The large load requirement for this application (500N) precluded the use of dead weight loading systems in the vacuum chamber, and the modular methodology described in the introduction precluded pneumatic and hydraulic loading/feedthroughs in the system. A relatively simple spring loaded system was selected to apply a normal force to the sample; such systems are typically avoided because creep and wear in the sample act to reduce the strain in the spring and the normal force is continuously decaying during operation. In this system the continuous measurement of normal force reduces these time varying biases. Additionally, very soft springs with the appropriate load capacities were selected to maximize spring deflections at load and thus minimize variations in load due to wear and other gradual deformations that occur in during testing.

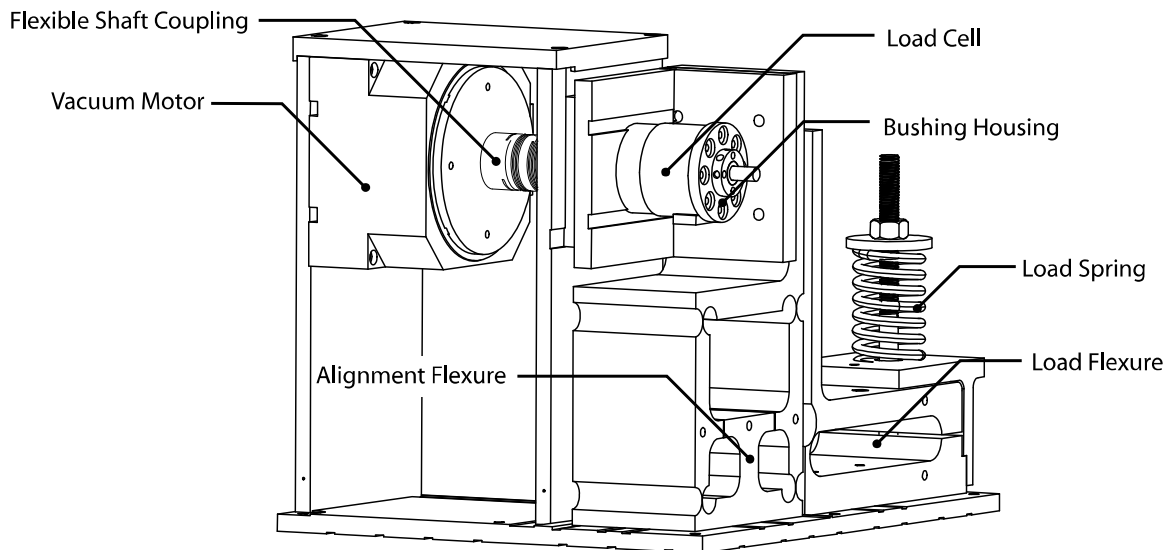


Figure 2-7 Bushing tribometer

Due to the challenges associated with maintaining low friction forces in vacuum environments, efforts were made to eliminate bearings and bushings in the design. The tribometer uses bearings only in the support of the rotating shaft and the motor. To apply normal load a series of two flexures act as a pivot to transmit the vertical load and as a restraint to force linear motion of the bushing in the loading direction. The load spring is compressed by tightening a nut on a threaded rod that is affixed to the load flexure. The alignment flexure is designed such that it can only move in the horizontal direction and imparts a purely horizontal load on the load cell and sample assembly through a point contact with a sphere. The function of the alignment flexure is to accommodate deflection during the wear of the bushing. The flexures were wire electro-discharge-machined from bulk monolithic stainless steel pieces.

The drive system for the shaft uses a high-vacuum compatible servo motor capable of running at speeds as low as 0.001 rpm and as high as 1000 rpm. The motor was originally designed to be cooled *via* convection. However, since this is not possible inside the vacuum system a chilled water circulator and aluminum block at the base of the motor are used to conduct heat out of the motor at high-vacuum levels. A flexible coupling is used to connect the motor to the rotating shaft and provides the opportunity to easily vary the diameters of the shafts. The shaft is aligned using two high vacuum rolling element bearings lubricated with fluorinated grease. These greases have very high molecular weights (3000+ AMU) with vapor pressures that are below 7×10^{-7} Torr at room temperature.

The entire bushing assembly is bolted directly onto to the front of the load cell to reduce uncertainties in the friction coefficient measurement. As described by Schmitz *et al.*(39), multi-axis load cell should be place directly in the load path between the sample and ground as close to the contact as possible. An illustration of the load path is shown in figure 2-9. All loads reacted

by the shaft are carried through the load cell, which is supported and constrained to linear motion by the alignment flexure assembly.

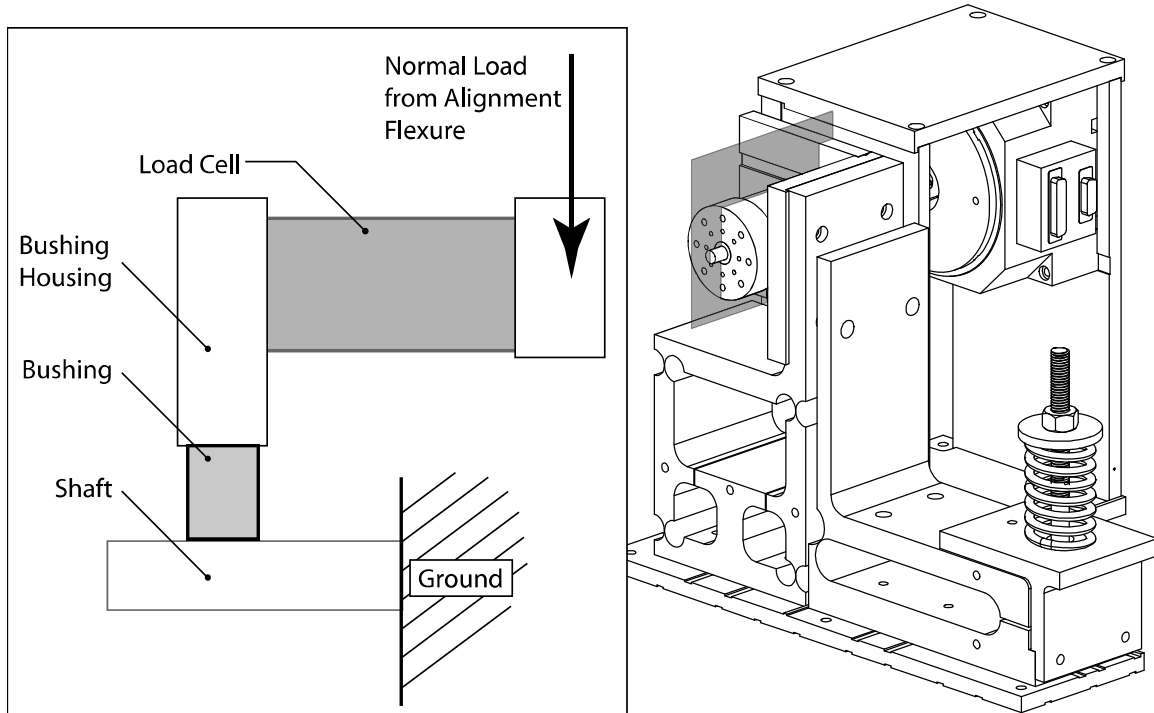


Figure 2-8 Illustration of load path to ground for bushing tribometer design.

There are a number of vacuum tribometers; however, the ability to perform cryogenic vacuum testing is much more limited. To reach temperatures below -100°C liquid nitrogen was fed through a cold flask within the vacuum chamber. This flask is mounted approximately 75 mm from the sample and thin copper braids are bolted from the reservoir to a copper bushing housing. This short conduction path and high thermal conductivities of copper made rapid cooling ($\sim 10^{\circ}\text{C}/\text{min}$) of the bushing assembly possible. To prevent cooling of the load cell, a polyetheretherketone (PEEK) insert is bolted between the copper bushing housing and the load cell as an insulator. The temperature is read from a thermocouple rigidly held to the outside of the bushing. The temperature rise across the bushing can be estimated using a simple 1-D heat

transfer analysis. The value for this temperature rise is 3°C using a 100 N normal load, 10 mm/sec sliding velocity and a friction coefficient of 0.5.(46)

Acquiring data during an experiment requires a card capable of reading multiple analog signals simultaneously. Using data acquisition all the different outputs (8) are read at up to 10 kHz for variable lengths of time. The ability to adjust acquisition rate and time is useful because the cycle time varies from one test to the next depending on the desired spindle speed. Typical settings for these options are an acquisition rate of 1,000 Hz per channel for a time period of six seconds. A majority of the tests run have been at 20 rpm, so the data is acquired for two complete cycles before being processed. All of the data collection is phase locked with the motor position. Plotting the force and torque values with respect to the motor's angular coordinate allows identification of persistent features. Any eccentricity between the shaft and bushing will manifest itself as a sinusoidal fluctuation in the normal force when plotted versus the angular position of the shaft. These fluctuations are by design small compared to the applied normal load.

This data collection scheme occupies a great deal of memory. The approach that is frequently used computes average cycle values from the kHz data and stores the average values in a single file. Periodically, the phase locked data is stored in a separate file that is time stamped with the cycle number. The distance value is calculated by using the input spindle speed, the shaft radius and the time the test has been running. This value has uncertainty because the values of spindle speed and shaft radius are assumed instead of monitored throughout the test, however, distance is not a factor in calculating friction coefficient. Schmitz *et al.* performed a rigorous uncertainty analysis on a system using the same electronics as the bushing tribometer

and found the contribution of the uncertainty from the electronics to be negligible when compared with other error sources.(39)

Computation of Friction Coefficient

The strain-gauge based load cell outputs forces and torques about all three axes, however, some of this information is not used in the computation of friction coefficient. In this tribometer, the two force values F_x and F_y are used to calculate the total normal force exerted on the shaft. The only torque that is of interest is the one generated by the friction between the shaft and bushing, thus only three of the six load cell channels are read into the software.

The friction coefficient is defined as the dimensionless ratio of the friction force between two bodies divided by the normal force pressing them together. The normal load exerted on the shaft by the bushing is measured directly, and the frictional stresses result in a torque. Assuming both the shaft and pin are rigid bodies (illustrated in the figure 2-10b) the normal load and friction force are assumed to be point loads and the standard friction coefficient equation, a ratio of the friction force to the normal force, is given by Equation 1.

$$\frac{F_f}{F_n} = \frac{T}{R_s \cdot F_n} \quad (2-1)$$

For two bodies in contact that are not infinitely stiff the contact area is finite due to deformation. This deformation introduces an error into the friction coefficient value reported by Eqn. (2-1). A simple model is to assume the shaft contacts the bushing over the bushing's entire length and the contact occurs over a specific wrap angle. Without more advanced material properties and contact mechanics, the exact wrap angle and pressure distribution cannot be determined. However, assuming a uniform pressure distribution over a contact area an analytical solution can be derived. For the case where the contact happens from $-\alpha$ to α , the normal load

measured by the load cell is the integrated contribution of the pressure distribution illustrated in Figure 2-10c.

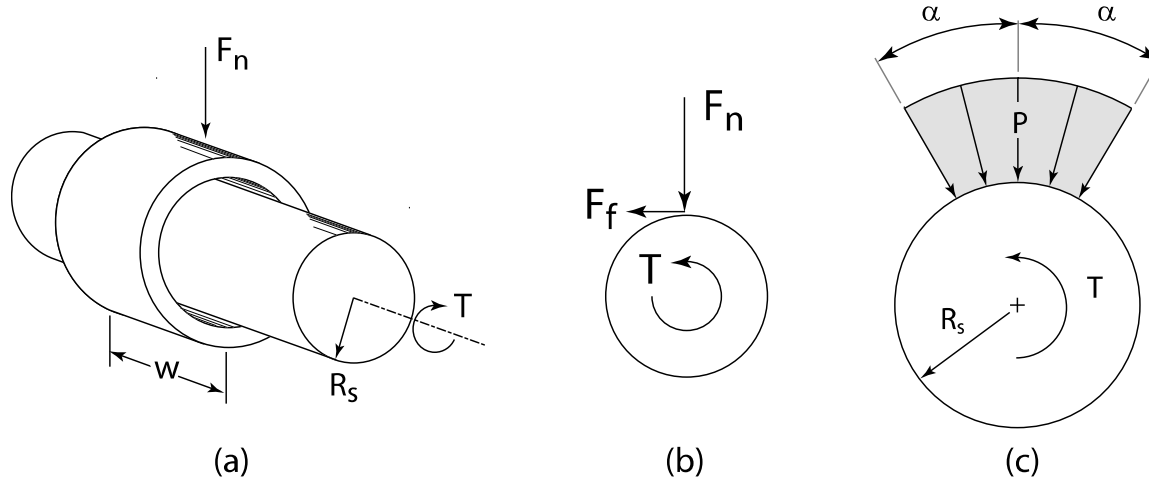


Figure 2-9 Friction coefficient derivation for bushing tribometer results.

The normal load measured by the load cell is a function of the length of the bushing (w), the radius (R_s), the pressure (p) and the contact angle (α).

$$F_n = 2 \int_0^{\alpha} p \cdot w \cdot R_s \cos(\theta) d\theta \quad (2-2)$$

The average pressure (p) can be calculated as a function of α given the measured normal load F_n .

$$p = \frac{F_n}{2 \cdot w \cdot R_s \sin(\alpha)} \quad (2-3)$$

The frictional shear stresses are simply the product of the friction coefficient (μ') and the normal pressure (p); thus, the frictional torque can be found from the following integral.

$$T = 2 \int_0^{\alpha} \frac{\mu' F_n}{2 w R_s \sin(\alpha)} R_s^2 d\theta = \frac{\mu' F_n R_s \alpha}{\sin(\alpha)} \quad (2-4)$$

Following Eqn. (2-1), the computed friction coefficient (μ) is given by Eqn. (2-5).

$$\mu = \mu' \frac{\alpha}{\sin(\alpha)} \quad (2-7)$$

For small wrap angle (α) the error is likely negligible, and the reported friction coefficient (μ) is always larger than the true value (μ'). A plot of the percent error (defined as $\%error = 100 \cdot (\mu - \mu') / \mu$) is shown in figure 2-11 illustrating that at a wrap angle of 20° the error in the reading is still below 5%.

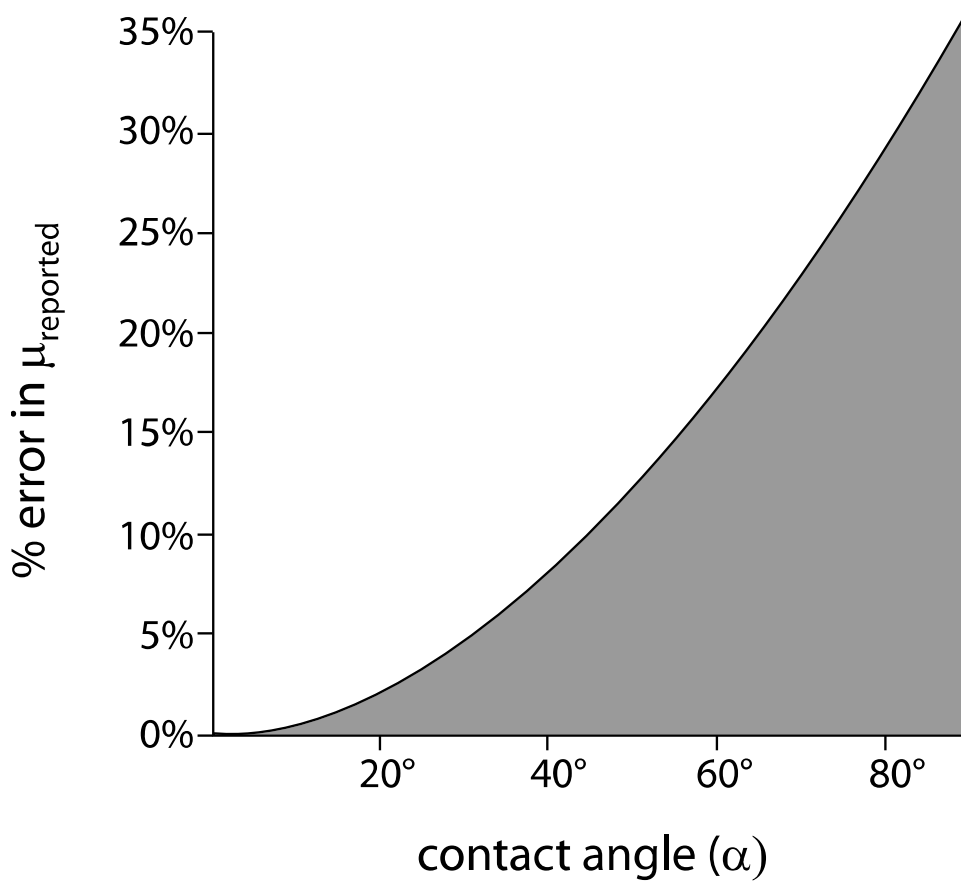


Figure 2-11 Error in friction coefficient based on the contact angle between the bushing and shaft.

CHAPTER 3
VARIABLE ENVIRONMENT EXPERIMENTS

3.1 Overview of Materials Used in Experiments

This series of experiments was meant to survey the field of possible coating options to determine their performance under varying environmental conditions. Groups from Harris Corporation, the Air Force Research Laboratories (AFRL) and the University of Florida were gathered to give input into the material selection for these tests. The coatings ranged from hard metallic coatings used in gears to intricate composite coatings designed specifically for low friction in varying environments. All coatings were applied to 1/4” spheres and 2” diameter disks of aluminum 7075. This substrate was chosen because it is common in many space mechanisms due to its high strength-to-weight ratio. The coatings were applied to both the pin and counterface to examine how the materials respond in a self-mated contact condition, as opposed to the coating against a nascent aluminum surface.

Table 3-1 List of coatings initially tested for environmental sensitivity

Group	Sample Composition	Sample Provider
Hard metallic coatings	Hard anodized aluminum	Hohman Coatings
	Electroless nickel	Hohman Coatings
	Titanium nitride with electroless nickel	Hohman Coatings
Metal coatings with PTFE	Hard anodized aluminum with PTFE	Hohman Coatings
	Electroless nickel with PTFE	Hohman Coatings
MoS ₂ -based coatings	MoS ₂ with Sb ₂ O ₃ and graphite	Air Force Research Labs
	MoS ₂ with Sb ₂ O ₃ and gold	Hohman Coatings
	MoS ₂ with Sb ₂ O ₃	Air Force Research Labs
	MoS ₂ with nickel	Hohman Coatings
	MoS ₂ with titanium	TEER Coatings
Bulk polymers	Bulk PTFE	University of Florida
	PTFE with PEEK and MoS ₂	University of Florida
	UHMWPE	McMaster Carr
Other	Near frictionless carbon	Argonne National Labs

Some of the coatings listed are commonly found in space applications, hard anodized aluminum with PTFE, MoS₂ with titanium, MoS₂ with Sb₂O₃ and gold, etc. The MoS₂ with Sb₂O₃ and gold coating was originally developed at the Air Force Research Labs, and has become a commercial standard for low friction interfaces in a variety of mechanisms. While many of the composites listed are commercially available they are not currently used in space applications and some are still in developmental stages (MoS₂ with Sb₂O₃ and graphite and near frictionless carbon). The purpose of this variety was to give designers insight into the performance of these new materials as possible options for future designs.

These coatings are created using a variety of different techniques. The anodized coatings are created by soaking the sample in a sulphuric acid bath while putting a current through the system. The coating forms about 2µm thick, while roughly 1µm of the sample material is removed leaving the sample oversized by 1µm. The electroless nickel process is a similarly bathed in solution. The system does not require electricity which reportedly reduces the friction coefficient over electroplated Watts nickel. Both of these coatings can be created with PTFE as a solid lubricant on the surface.

3.2 Cryogenic Pin-On-Disk Experiment

Environmental Protocols

Reducing the temperature of any surface at atmospheric pressure (as opposed to vacuum) can form water on that surface as water vapor in the surrounding environment comes out of solution and condenses. When performing experiments at reduced temperatures it is important that the test be run above the dew point for the water vapor in the atmosphere to avoid confounding the tribological results by forming water at the interface. As the surface temperatures decrease, the amount of water vapor required for condensation to occur decreases. To combat this problem, it is necessary to remove as much water from the surrounding

environment as possible. The enclosure used in this experiment was a Vacuum Atmospheres environment chamber, which isolated the experiment from ambient humidity. This chamber was backfilled with ultra-high purity nitrogen gas (99.999% pure) as well as boil-off from liquid nitrogen dewars to remove as much water vapor from the system as possible and create an inert environment with controlled relative humidity levels around the tribometer. The environment chamber was also fit with a humidity sensor by GE Sensing capable of resolving relative humidity less than 0.1%.

Inside the chamber, a technique similar to that used in metal inert gas (MIG) welding was employed to keep the surface of the disk as cold and clean as possible. Liquid nitrogen flows from a pressurized dewar through braided steel lines to a nozzle located above the disk surface. The liquid nitrogen flows from the nozzle two inches above the disk surface nearly parallel to the plane of the disk. Another jet of nitrogen from an ultra-high purity nitrogen cylinder is pointed down onto the center of the disk. The flow rate of this jet is controlled by an adjustable flow controller to increase or decrease the amount of gas impinging on the surface. The two jets intersect above the disk surface causing the liquid nitrogen to volatilize into cryogenic nitrogen gas which is carried to the surface by the impinging gas nitrogen jet (see Figure 3-1). Using this method, surface temperatures could be controlled down to -80°C . To increase the temperature of the surface, a heat gun was mounted above the disk surface impinging directly onto the center of the disk. The temperature of the disk surface was increased as high as 180°C during the testing. In both cooling and heating, it was important to keep the gas flow near the center of the disk because any viscous flow off-axis to the load armature could affect normal force and or friction force.

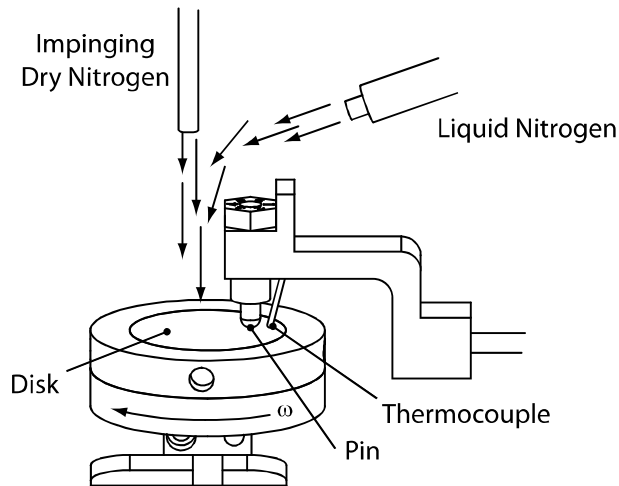


Figure 3-1 Description of impinging jet technique used to cool and clean the surface of the disk during experiments.

Experimental Procedure

The pin-on-disk experiments conducted on the Falex instrument were run at the lowest obtainable relative humidity levels (below 1% for all the experiments). A 500 gram dead-weight load was hung from the armature on the tribometer resulting in a nominal normal load of 2.5 N at the pin. Each sample was tested at three separate temperatures -70°C, -30°C and 20°C. Fresh tracks were used for each test to eliminate the possibility previous temperature affecting the results. The procedure for each new track was to run the sample in at room temperature to wear through any oxide layers that may have formed on the surface between deposition and experiment. After the friction coefficient reached a steady-state, the test was stopped and the temperature of the system was reduced to the target value. The temperature was held near the target for several minutes prior to beginning the test to ensure both the disk and ball were equilibrated. Once the system was at the target temperature, the motor was started and friction coefficient recorded for a period of five minutes or more. This was to ensure there were no transient behaviors in the friction coefficient and there was enough data minimize the effects of noise in the system. The sliding speed for the innermost track on the sample was 12.5 mm/sec (5

mm radius at 50 rpm), but the sliding speed increased as the track diameter increased because the motor was unable to reliably spin the disk at speeds less than 30 rpm. The maximum sliding speed for the samples at the outermost track was 30 mm/sec (10 mm radius at 30 rpm). Johnson et al. showed friction coefficients for MoS₂ coatings were relatively insensitive to sliding speed over this range.(10) The steady-state temperature rise in the system can be estimated using a simple 1-D conduction equation.(46)

$$\Delta T \sim \frac{\ddot{q}a}{K} \quad (3-1)$$

To use this equation, the nominal contact radius and the heat flux must be calculated. The contact radius (a) can be estimated using a Hertzian contact solution. For a sphere on flat contact, the equivalent radius of the two bodies is equal to the radius of the sphere.

$$\frac{1}{R} = \frac{1}{R_a} + \frac{1}{R_b} = \frac{1}{R_a} + \frac{1}{\infty} \quad (3-2)$$

The composite modulus for the bodies is calculated using the modulus and Poisson's ratio for both bodies.

$$E' = \frac{E_a \cdot E_b}{E_b(1-\nu_a^2) + E_a(1-\nu_b^2)} \quad (3-3)$$

Using these values, the contact radius can be calculated given a normal load.(47)

$$a = \left(\frac{3F_n R}{4E'} \right)^{\frac{1}{3}} \quad (3-4)$$

The heat flux generated is a function of the average contact pressure, the friction coefficient and the sliding velocity.

$$\ddot{q} = \mu \cdot \bar{P} \cdot v \quad (3-5)$$

In the given experiments, a worst-case scenario for friction coefficients was on the order of 0.5. The highest recorded sliding velocity was 30 mm/sec, and the normal load was 2.5 N. Given all these values, the contact radius and heat flux can be calculated.

$$a = 0.0515\text{mm} \quad (3-6)$$

$$\dot{q} = 4.5\text{W}/\text{mm}^2 \quad (3-7)$$

The resulting steady-state temperature rise for these contact conditions is less than 1°C (0.966°C). In the case of the solid lubricant films, the friction coefficients were an order of magnitude lower than the example; indicating the temperature of the system before motion and after motion should be equivalent.

After running the experiments at reduced temperatures, the materials that displayed a strong sensitivity to temperature were tested at an elevated temperature of 180°C using the same procedure described above. This was done to evaluate how much of a reduction could be seen at elevated temperatures.

3.3 *In Situ* Wear Experiment

The friction response of MoS₂ coatings in dry (RH less than 1%) environments and high vacuum has been well documented. Since the discovery of this material more than 60 years ago, different techniques have been developed for applying a MoS₂ coating, different additives have been mixed with MoS₂ to improve its friction response and its surface adhesion. However, the wear analysis of this coating has been very limited. A majority of the studies where wear volume is quantified report values determined *ex situ* and usually after the coating has failed. The purpose of this experiment was to capture the evolution of the wear scar as the test progressed, and determine a correlation between friction coefficients and wear rates.

The tribometer used in this experiment was a linear reciprocating tribometer mounted underneath a Zygo New View 5030 scanning white light interferometer. Although the resolution of the device is on the order of angstroms, the device is capable of detecting surface topography changes on the order of nanometers. The general idea behind this experiment is to image a section of the wear track at different cycles throughout the test to estimate a volume loss and a wear rate.

Sample Description

The counterface samples used were nominally 1.5" x 1.0" x 0.1875" coupons made of 304 stainless steel. The coupons were polished on a polishing wheel to a surface roughness less than 50 nm prior to being shipped to the suppliers for coating. The pin samples were ¼" 6061-T6 aluminum spheres that were drilled and tapped for a 4-40 screw. No surface preparation was done to the spheres prior to coating. The coatings applied to the pins and coupons were all MoS₂ based, but had a variety of other constituents. The commercially available coatings used were MoS₂ with titanium, MoS₂ with Sb₂O₃ and gold, and MoS₂ with nickel. The newly developed coatings from the AFRL were MoS₂ with Sb₂O₃ and one of the "chameleon" coatings (MoS₂ with Sb₂O₃ and graphite). All coatings were nominally 1 μm thick, although each one was deposited using different techniques. The MoS₂ with titanium is a layered coating created by sputtering a layer of pure titanium on the surface of the substrate, then co-depositing a layer of MoS₂ and titanium, then a layer of pure MoS₂. The MoS₂ with nickel and the MoS₂ with Sb₂O₃ and gold coatings are sputtered coatings of MoS₂ with other constituents to improve adhesion to the substrate, environmental sensitivity and toughness. The AFRL coatings are created by laser ablating a target made of the desired constituents resulting in a coating with roughly the same composition as the target.

Environmental Protocols

There were two environmental protocols used to test these coatings. The first was a cycling environment similar to the ‘pump and purge’ experiments described in the high vacuum pin-on-disk experiments; in these experiments the acrylic chamber surrounding the tribometer was back-filled with dry nitrogen to a relative humidity less than 2%. The sample was run for a total of 500 cycles in this environment and surface scans were taken at 1 – 20, 30, 40, 50, 100, 200, 300, 400 and 500 cycles. The chamber was then purged with laboratory air (RH > 20%) and the sample was run for another 500 cycles using the same scanning frequency. This process was repeated once more for a total of 2000 cycles. The hope was the data would provide insight into how the system wears in the transition between a dry environment, where friction coefficients were below 0.05, and a humid environment where friction coefficient was above 0.1. Experiments were run starting in nitrogen or humid air to see if the initial run in affected the future performance of the coating.

The second procedure was aimed at determining a steady-state wear rate for each coating in a dry nitrogen environment and a humid air environment. Two separate tracks were run on each sample. The first track was run in dry nitrogen at a relative humidity of less than 1%. The second was run in laboratory air at a relative humidity of greater than 20%. Each sample was run for a total of 10,000 cycles and images were taken every 1000 cycles. The chameleon coating from the AFRL was the coating of interest in this experiment primarily because it is hypothesized that the coating draws the favorable solid lubricant to the surface of the film based on environment. If this theory is correct, the track run in air should have a higher carbon signature than the one run in nitrogen because the graphite in the material is designed to be the solid lubricant in the moist environment. Appendix C shows the results of Auger electron spectroscopy run on the Chameleon coating and the MoS₂ with titanium coating.

Experimental Procedure

Before any testing could begin with the coated samples, a calibration step was taken to ensure the objective lens of the Zygo was aligned with the wear track, and to determine the distance between the Zygo lens and the pin holder. An uncoated counterface and pin were mounted to the system and the counterface was moved under the Zygo objective. The roll and pitch of the Zygo stage was adjusted to align the counterface normal with the objective axis. After the surface was brought into focus, the stage was returned to its initial position and the pin was loaded to 5 N. The sample was then run for 50 cycles on a 5 mm track to ensure a noticeable wear scar was generated. The pin was unloaded and brought up from the sample surface. The stage was jogged 0.5 mm at a time until the scar was inside the field of view of the Zygo lens. The Zygo stage was adjusted in the x-y plane to bring the end of the scratch into the center of the field of view of the Zygo. The distance between the pin and lens was then determined and recorded for future use during the experiment.

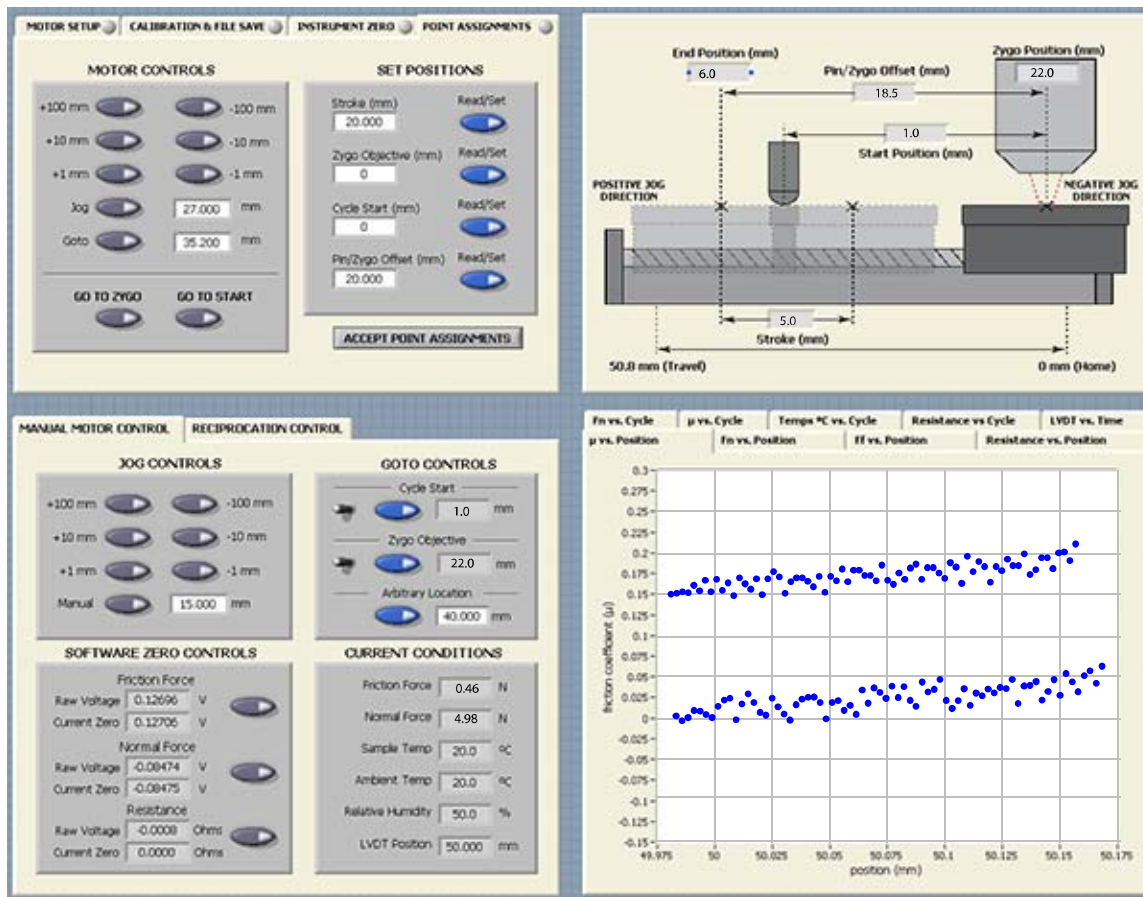


Figure 3-2 Screenshot of LabView software written for the in situ wear experiments.

When calibration was complete the sample counterface was bolted to the motorized stage. The coated aluminum pin sample was screwed to the PEEK housing and the housing mounted to the load cell. At this point, the LabView software was opened to begin the experiment. Inside the software there are several steps required to begin a test.

1. Enter the calibration constants for the load cell, thermocouples, humidity sensor and positional encoder.
2. Set the location for data files to be saved and enter any notes on the pin and counterface samples
3. Tare the load cell

4. Define the absolute motor positions of the Zygo objective lens, the track start point and the track end point so the motor can be commanded back to those positions for the duration of the experiment
5. Move the sample under the Zygo objective and record the cycle 0 image of the track. This image represents the unworn surface topography and will be used to make all the differential volume loss calculations.
6. Command the sample back to the cycle start position.
7. Bring the pin sample into contact with the surface and adjust the micrometer stage to apply the appropriate load (in this case 5N).
8. Define the track length, sliding velocity and approximate cycle time for the test, 5mm, 10mm/sec and 1.0 seconds respectively.
9. Enter the data acquisition parameters (sampling period of 1.1 seconds and sampling frequency of 1 kHz)
10. Define how often the software saves a complete cycle of positional data as opposed to simply an average value for a cycle.
11. Enter the position of the center point of the wear track and the percentage of the wear track to analyze (this is to avoid using the data at the reversal points in the average friction calculations)
12. Begin the test.

During these experiments, the LabView software recorded normal force, tangential (friction) force, ambient temperature, relative humidity and stage position. As mentioned, the software periodically records the phase-locked data associated with a single cycle. Phase-locked data refers to a correlation between the values recorded, specifically friction force and normal force, and the stage position. This can be most useful for initial run in or the onset of failure when a single cycle can be evaluated to look for a portion of the track that is anomalous. Ultimately the goal of the instrument is to identify portions of the track with erratic behavior and be sure to image them to give some insight into the failure mechanisms of the coatings.

Following completion of the test, the samples were removed from the tribometer and vacuum sealed to help protect the surfaces from contamination and oxidation. Two of the coatings were evaluated using Auger electron spectroscopy to try and identify the composition of the surfaces after wear occurred.

3.4 Cryogenic High Vacuum Bushing Experiment

Environmental Protocols

Relating friction results obtained using a tribometer in a laboratory environment to actual frictional losses in a mechanism is not straightforward. Bridging the gap between contrived experiments and real world environments is a primary goal for many researchers. To that end, experiments were run using the cryogenic high vacuum bushing tribometer described in chapter 2.4. The purpose of these tests is to compare results obtained at cryogenic temperatures on a pin-on-disk tribometer with frictional torques generated in a bushing-shaft contact under similar conditions.

The simulation of a space environment has a broad definition; in this experiment a high vacuum environment over a range of temperatures are the target conditions. The vacuum level of 1×10^{-6} Torr was chosen as the required pressure level prior to starting the test. At this pressure, the monolayer formation times are on the order of one second, meaning a single layer of molecules (usually water) will adsorb on any available surfaces in roughly one second. The vacuum pumps continue to work throughout the experiment and can reach levels below 1×10^{-7} Torr. The point of this pressure range is to ensure that the shaft is not covered with more than a monolayer of contaminant while it is not in contact.

The temperature profile used in these experiments is a ramp that begins at room temperature (20°C) decreases linearly to -60° and then steadily increases back to room temperature. Throughout the course of this temperature ramp, data points are taken at 20°C,

0°C, -20°C, -40°C, -60°C, -40°C, -20°C, 0°C and 20°C. Although data is collected the entire time, thermal drift in the system can only be eliminated using reversal techniques. The purpose of taking data on the reduction in temperature and the increase in temperature is to ensure that friction response is due to a temperature effect and not to unrecoverable damage to the coatings.

Material Preparation

The bushings used for these experiments were 440C stainless steel with a 10.0 (+0.05/-0.00) mm inside diameter. The shafts were made of custom 455 stainless steel; they were 8” long and had a 10.0 (+0.00/-0.05) mm outer diameter. The nominal clearance between the shaft and bushing was 0.05 mm in all cases. All the shafts were polished to a surface roughness of less than 100 nm prior to being sent out for coating. Both the bushings and shafts were coated with the same material to mimic the self-mated contacts of the pin-on-disk experiments. Only a subset of the MoS₂ coatings were chosen for the bushing experiments mainly to verify the temperature sensitivity of the coatings in an application specific contact geometry. The most sensitive coating (MoS₂, Sb₂O₃ and gold), the least sensitive coating (MoS₂ and nickel) and an intermediate coating (MoS₂ and titanium) were used to coat bushings and shafts. All three of the coatings are commercially available and commonly found in high vacuum environments.

Experimental Procedure

The process followed for the cryogenic high vacuum bushing experiments was outlined by the Harris Corporation. This protocol was also used in the fluorinated grease experiment mentioned earlier. The procedure for each test was:

1. Open the high vacuum chamber.
2. Load the shaft into the alignment bearings
3. Couple the shaft to the vacuum motor
4. Attach the bushing housing to the load cell

5. Tare the load cell
6. Insert the bushing into the housing
7. Open the LabView software written for the experiment
8. Enter the calibration constants for the load cell, motor encoder, pressure gauge and thermocouples
9. Define the location the data files are to be saved
10. Apply the normal load to the bushing
11. Close the chamber
12. Evacuate the chamber to high vacuum
13. At the desired pressure, run 5 revolutions in the forward direction and 5 revolutions in the reverse direction. The average value determines any misalignment or drift in the torque cell.
14. Begin the test.
15. At each temperature run the bushing in a clockwise direction to steady-state and then reverse the motor direction and again run to steady state. This allows for an accurate assessment of frictional torque and reduces the influence of drift.

The bushing was run to a steady-state friction value at room temperature. Once a friction coefficient was determined at room temperature, the motor was stopped. The liquid nitrogen was turned on and the indirect cooling system began to reduce the temperature of the bushing housing and the bushing itself. A thermocouple placed against the outside edge of the bushing was used to estimate the temperature in the contact. After the temperature on the thermocouple reached the desired running temperature, the motor was started. The friction was run into a steady-state value while the temperature was held relatively constant (fluctuations on the order of $\pm 5^{\circ}\text{C}$). The temperature profile for the system was 20°C , -60°C , -20°C , 0°C , 20°C .

CHAPTER 4 RESULTS

4.1 Cryogenic Pin-On-Disk Experiment

Determining a Friction Coefficient

The calculation of a friction coefficient value for each temperature was accomplished by determining the steady-state value of the friction coefficient data over a period of time where the temperature of the system had reached equilibrium and remained constant. The purpose of this technique was to eliminate transients in the friction response due to fluctuating temperatures. The mean and standard deviation of the friction coefficient values were calculated for all the data collected in this period to quantify the consistency of the friction. For cases where the surface was plastically deformed and/or large amount of debris were generated, the spread on the data tended to be large compared to the value itself. The solid lubricants, on the other hand, tended to have a consistent friction response with small standard deviations given a constant temperature.

Experimental Results

The thermal response of materials is a primary concern for designers of equipment for space applications mainly because the operating range for some of these mechanisms is -100°C to 200°C . This large range of operating temperatures causes engineers to consider thermal effects that may not ordinarily be problematic. One such issue is the mismatch of coefficient of thermal expansion between dissimilar metals. This mismatch can distort the geometries when the system experiences temperature fluctuations on the order of several hundred degrees. Another commonly overlooked property is the friction response of a material as the temperature fluctuates. Many designers view friction coefficient of a material as a property of the material and not a value that is strongly influenced by geometry and environment. These experiments began with an experiment performed at the University of Florida using thin PTFE composite

coatings indicating a sensitivity of friction to temperature.(6) While this result is not widely accepted, and others have published data to the contrary, it lead to the idea that other materials might also display such a response.(48)

The first coatings evaluated in this experiment were hard metallic coatings. The temperature of the samples was decreased from room temperature down to 200K (-73°C). An example of the friction result is plotted in figure 4-1. This is the result for the electroless nickel coating, and indicates the degree of scatter in the data. Each data point on the plot represents the average value for multiple cycles of data. These results are representative of all the hard metallic coatings tested, and there was no indication that temperature affected the friction response.

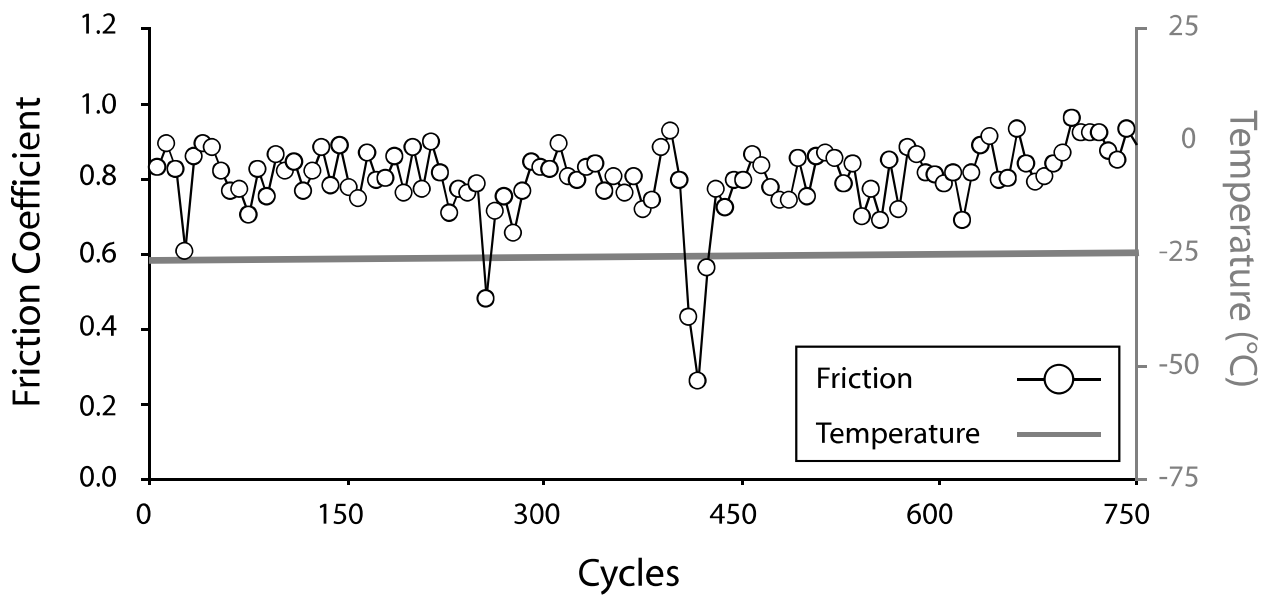


Figure 4-1 Friction plot of the electroless nickel coating at -25°C. The plot indicates the large fluctuations in friction coefficient throughout the experiment. The average value for this data was $\mu = 0.8$ with a standard deviation of 0.1. The temperature of the system is also plotted to indicate the small fluctuations in temperature over a 15 minute period.

The erratic behavior of the friction of each of the metallic coatings coupled with small changes in the friction coefficient over the range of temperatures tested lead to the decision that no higher temperature testing was warranted for these coatings. There was no indication that the

plastic deformation or abrasive wear of metallic coatings responded to temperature fluctuations. While this result is not particularly interesting, it provided an important null result; which was the tribometer itself had no inherent bias resulting from a varying temperature. This can be seen from the fact that although the temperature of the system changed by 100°C, the responses from each of the metallic coatings stayed constant and those values were unique to each coating.

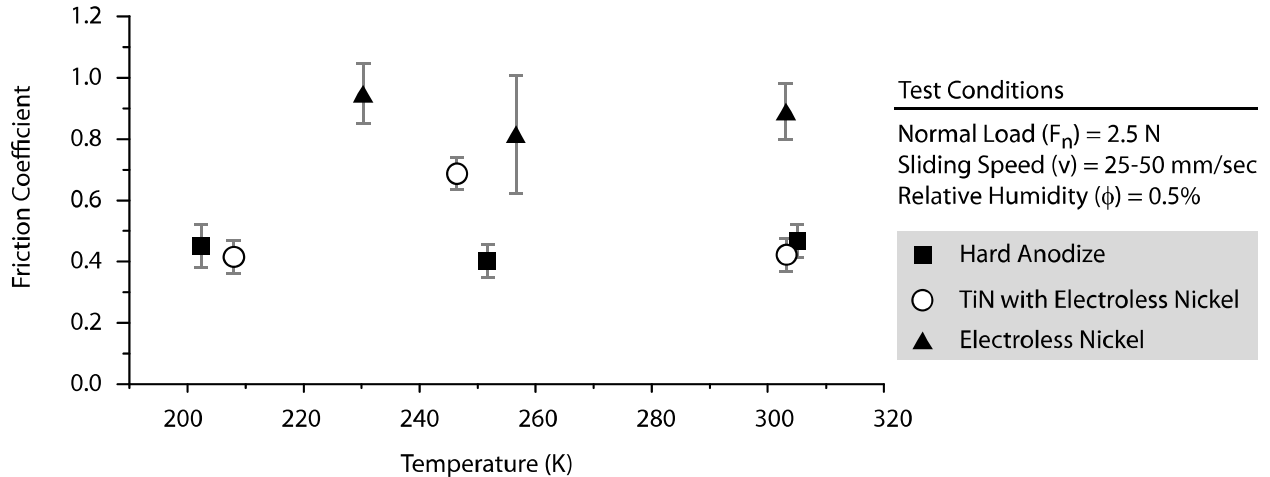


Figure 4-2 Friction response of metallic coatings to varying temperature. The friction forces were scattered due to the large amount of surface deformation and wear that occurred during the test.

While metallic coatings are commonly used in gear teeth because they are known to be hard and tough, they are also known to have high friction. One method for improving the performance of these coatings is to deposit a solid lubricant with the coating. Two of the above-mentioned metallic coatings are also available with PTFE impregnation. The hard anodize and electroless nickel coatings are commercially available with PTFE. The manufacturers claim these coatings are highly wear resistant, and the addition of a solid lubricant greatly improves the friction performance of the coating. These coatings were tested following the same procedure as the metallic hard coatings to explore the thermal sensitivity. Like the metallic coatings, there was little evidence to support a thermal sensitivity in the results from these coatings. There is,

however, evidence to support the addition of PTFE greatly decreases the friction coefficients of these coatings.

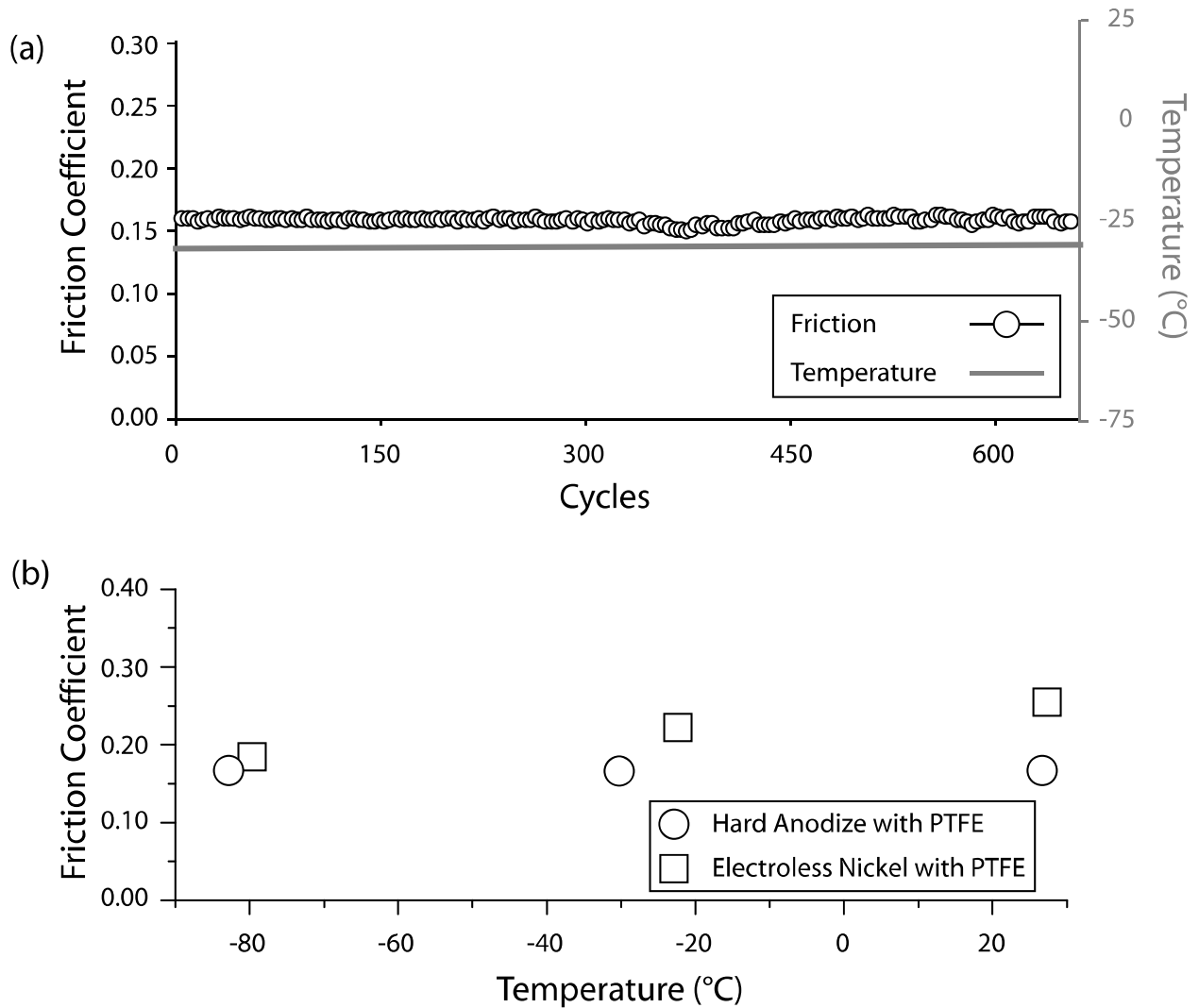


Figure 4-3 Friction response of metallic coatings with solid lubricant impregnated. (a) The friction results for hard anodize with PTFE coating at -30°C. (b) The friction results for the metallic coatings impregnated with PTFE were much more uniform than the metallic coatings alone, but the coatings did not appear to be sensitive to changing temperatures.

Bulk polymeric components can also be used in mechanisms designed for high vacuum such as bushings, snaps and pins. These materials tend to be very inert and have low outgassing rates.

The bulk polymeric materials tested in these experiments were PTFE, UHMWPE and a PEEK/PTFE. Unlike the coatings tested in these experiments, these samples were run against

stainless steel pins. Although the contact does not start out self-mated, polymeric samples readily form transfer films on the steel surface so after a short run-in period they are essentially running in a self-mated configuration.(49)

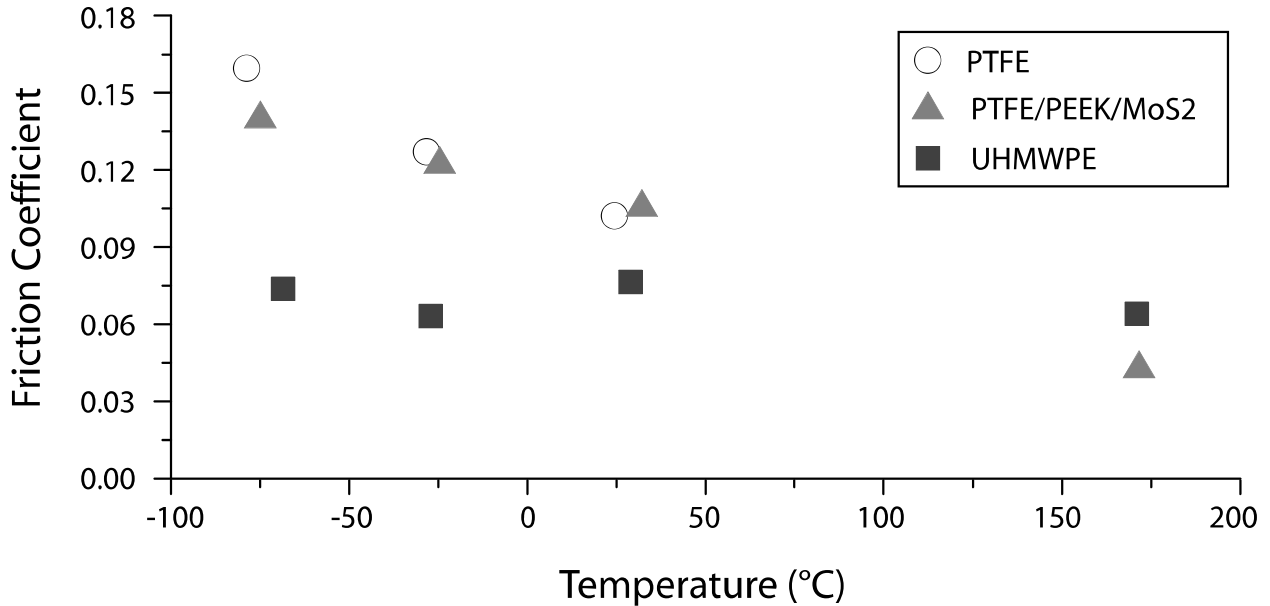


Figure 4-4 Results for bulk polymeric samples against a stainless steel pin. The PTFE-based samples displayed a linear decrease in friction coefficient with increasing temperature, while the UHMWPE sample maintained a constant friction coefficient regardless of temperature.

The PTFE and PTFE/PEEK/MoS₂ composites both demonstrated a linear trend of decreasing friction with increasing temperature. Unfortunately, there are so many properties of PTFE that change with temperature; it is possible to generate a number of explanations for this result. The UHMWPE, on the other hand, did not show a discernable trend of friction with temperature. As with the metallic coatings, this is further proof that the system is not inherently sensitive to temperature.

In contrast to all the previous results, many of the MoS₂ based coatings were very sensitive to temperature fluctuations. MoS₂ with nickel was the least sensitive, and reacted similarly to the PTFE based composites. The trend for this coating was nearly linear with temperature. The

MoS₂ with titanium and the MoS₂ with Sb₂O₃ both had a friction coefficient of 0.05 at room temperature and increased by 300% as the temperature dropped to -70°C. The MoS₂ with Sb₂O₃ and graphite had a friction coefficient below 0.03 at room temperature, but increased to over 0.15 at -70°C. In the most extreme case, that of MoS₂ with Sb₂O₃ and gold, the friction increased by an order of magnitude from 0.02 to 0.2 over the 100°C temperature drop.

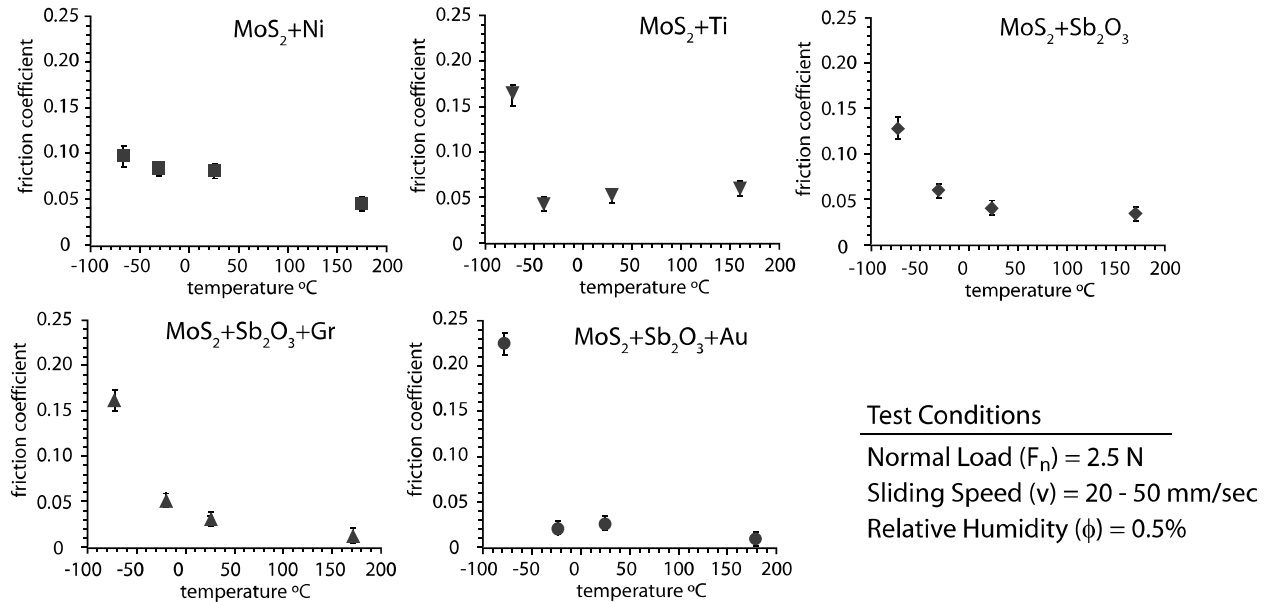


Figure 4-5 Friction coefficients of MoS₂ based solid lubricant coatings at varying temperatures. The nearly pure MoS₂ with nickel coating (95% MoS₂, 5% Ni) had the lowest sensitivity to temperature. The commercially available MoS₂ with Sb₂O₃ and gold had the lowest recorded friction at 180°C and the highest increase in friction as temperature decreased (over an order of magnitude).

One observation of note was that the materials with the lowest friction coefficient, and highest thermal sensitivities did not have noticeable wear scars. This is in contrast to the metallic coatings that exhibited high friction coefficients, no thermal sensitivity and large amounts of debris generation. The differences in wear debris and wear track generation sparked an interest in studying the evolution of the wear scars *in situ*.

4.2 *In Situ* Wear Experiment

The *in situ* experiments performed in a changing environment provided some insight into the surface topography changes of MoS₂ based systems that accompanied changes in humidity. While an increase in humidity immediately triggered an increase in friction, the surface topography did not react as quickly. In fact, the wear mechanism described by Spalvins where the columnar growths within the film shear and break leaving a well-adhered, thin layer of composite seemed to be accurate for the MoS₂ and nickel coating.(21) The other composite coatings where the structure is intentionally amorphous seemed to deform initially under loading and shear stress, but stabilize quickly to a low wear configuration. Another attribute of the composite coatings is the presence of additive materials. These other constituents (e.g. titanium or Sb₂O₃) are thought to improve the quality and toughness of the coating and prevent the columnar growth of the film.

Estimating the wear volume given the topographical information of a section of the wear scar required a technique initially introduced by Williamson and Hunt, and refined by Sayles. In the original publication from Williamson and Hunt, the technique was used to evaluate the persistence of asperities after plastic deformation had occurred.(50) Sayles expanded the technique to evaluate a surface before and after plastic deformation.(51) The method uses an initial surface topography scan as the basis for the wear scar and takes subsequent topography scans to calculate the cross sectional area of the wear scar. Using this area extrapolated over the length of the scratch, a volume loss can be estimated. This method was followed for all the coatings tested in both the alternating environment experiments and the steady-state wear rate testing.

The wear rates reported in this section were obtained using a methodology originally developed by mathematician Stanislaw Ulam for predicting odds for the appearance of various

cards in games of solitaire.(52) The technique was named Monte Carlo simulation for Ulam’s uncle, who was a known gambler. The Monte Carlo simulation style is suited to systems that are dominated by random events or where no analytical solution can be found. The technique uses random number generation to predict how a ‘random’ system will react to different inputs. The reaction is simulated a large number of time and the statistics of the results are considered the odds of one result or another. For the wear rate data, each data point on the graph represents an interrupted measurement. Using an estimation of the uncertainty in this measurement and random numbers, new data points were generated. For each data set, 1,000 possible sets were generated and a linear fit was used to calculate a wear rate for each. The average wear rate value was the wear rate calculated from the original data points, and the uncertainty in that wear rate was the standard deviation of the 1,000 wear rates calculated from the generated data. This procedure was followed for all the wear rates calculated in these experiments.

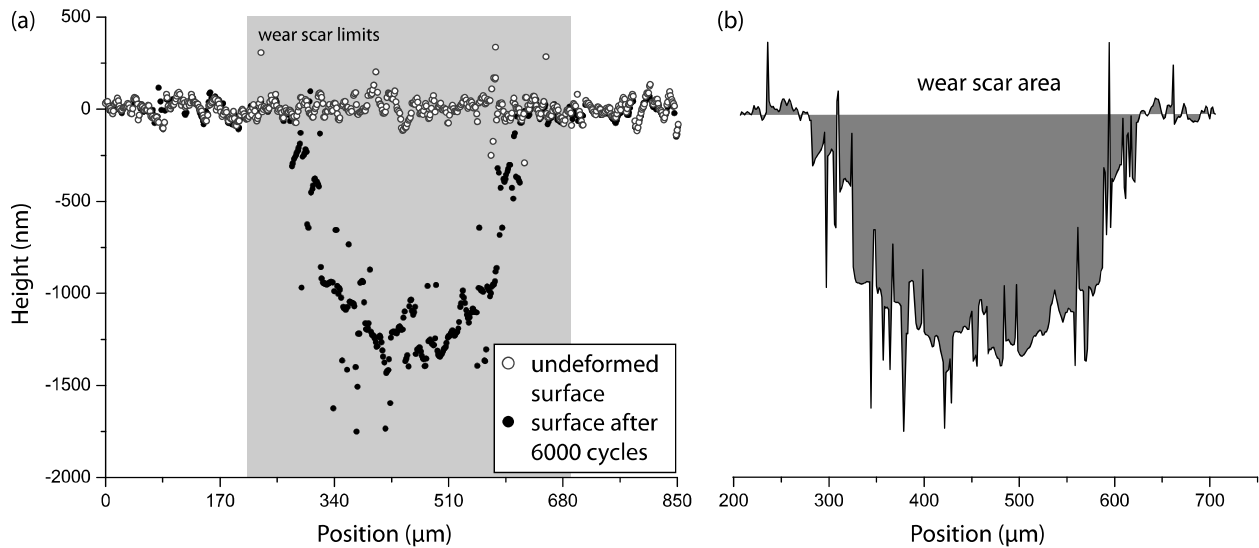


Figure 4-6 Methodology for calculating wear volume. (a) Plot of a line scan taken from the undeformed surface scan made by the Zygo prior to beginning the experiment and a line scan taken from the surface scan made after 6,000 cycles. (b) Estimation of the wear scar cross-sectional area using the difference between the two line scans. This area is multiplied by the length of the track to estimate a wear volume.

By alternating the environments it was possible to determine if the wear rate of the coatings reacted to the environment as the friction coefficient obviously changed. In a majority of the coatings, it was found that even though friction coefficient changed dramatically, the wear rate of the systems was not affected. The only coating that demonstrated a noticeable and repeatable change in the wear rate with environmental changes was the MoS₂/titanium coating. This coating showed a lower wear rate in dry nitrogen when compared with humid air. The coating also wore more readily when transitioning from a dry environment to a humid environment.

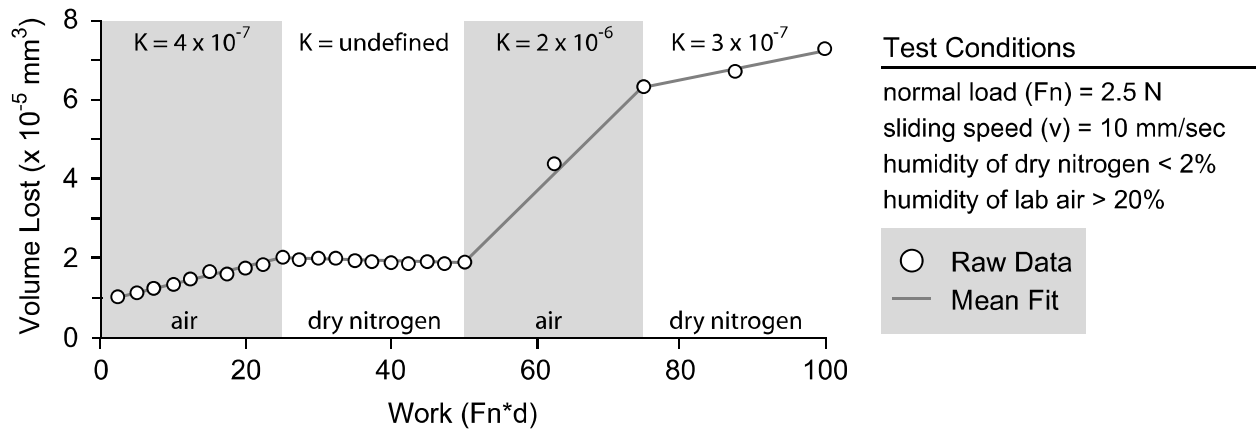


Figure 4-7 Plot of volume lost vs. work input into the system. The plot indicates the wear of this coating is sensitive to the partial pressure of water in the environment. In this case, the wear rate initially in air is much less severe than transitioning from a dry environment to a humid one.

Many of the other coatings did not show appreciable changes in wear rate in varying environments. For example, the MoS₂ with Sb₂O₃ and gold showed no evidence of different wear regimes throughout the 2,000 cycle test regardless of environment. This sample had a wear rate of 5×10^{-8} mm³/Nm, but the uncertainty in this value was nearly 100 percent. The deepest penetration depth on this coating throughout the test was 80nm, and the repeatability of the instrument is estimated at 10nm. One explanation for the large uncertainty is the methodology used for estimating wear volume was not sensitive enough to reliably capture surface topography

changes that are on the order of 5nm. To increase the wear volume the number of cycles was increased to 10,000 in each environment and the normal load was increased to 5N. This allowed for the calculation of a steady state wear rate in humid air and dry nitrogen to discern if the environment had any effect.

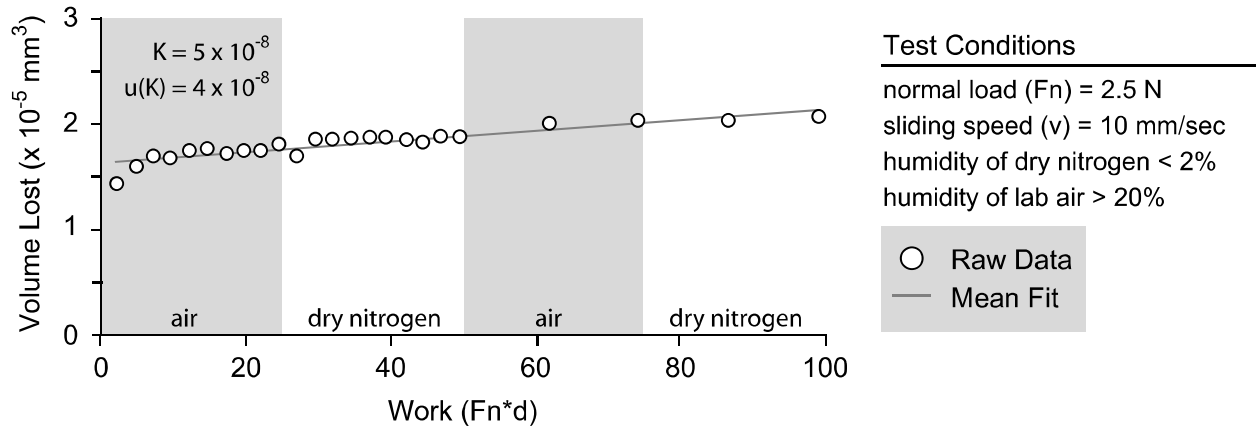


Figure 4-8 Plot of volume lost vs. work for the MoS₂ with Sb₂O₃ and gold coating. The uncertainty in this value is nearly 100% of the value due to the small volume loss over the course of the entire 2,000 cycles. This result led to testing at higher normal loads and larger numbers of cycles.

The 10,000 cycle experiments were aimed at determining a steady-state wear rate in humid air and dry nitrogen. The hope was to determine if environment had any effect on the generation of wear debris. In a graphite system, the lack of humidity causes the graphite to become brittle and wear more rapidly. It was expected that MoS₂ based systems would demonstrate a similar behavior when exposed to a humid environment. This hypothesis proved to be correct in every case where MoS₂ was the only solid lubricant present in the system. The wear rates for all these coatings were lower in dry nitrogen than it was in humid air. Only the MoS₂ with Sb₂O₃ and graphite demonstrated a consistent wear rate regardless of the environment. This coating is also the only one with a constituent solid lubricant suitable for both environments. The theory that graphite is drawn to the surface during sliding in humid environments is supported by the Auger analysis in Appendix C. The signature from MoS₂ in the track was much stronger in the dry

nitrogen track than it was in the humid air track. Only carbon and oxygen had significant peaks in the wear track run in humid air. The results for all the steady-state wear studies are shown (Table 4-1). The uncertainty values listed are the values from the Monte Carlo simulations; however, based on the sensitivity of the instrument the minimum uncertainty that should be expected is $1 \times 10^{-7} \text{ mm}^3/\text{Nm}$.

Table 4-1 All the steady state wear testing in humid air and dry nitrogen.

Coating Material	K_{humid air} (mm ³ /Nm)	u(K) (mm ³ /Nm)	K_{dry nitrogen} (mm ³ /Nm)	u(K) (mm ³ /Nm)
MoS ₂ with nickel	2.51×10^{-5}	1.10×10^{-6}	7.44×10^{-6}	1.10×10^{-6}
MoS ₂ with Sb ₂ O ₃	9.18×10^{-7}	1.10×10^{-7}	5.32×10^{-7}	1.90×10^{-8}
MoS ₂ with titanium	4.23×10^{-6}	3.20×10^{-7}	7.21×10^{-7}	1.00×10^{-7}
MoS ₂ with Sb ₂ O ₃ and graphite	1.75×10^{-8}	2.20×10^{-9}	2.29×10^{-8}	4.40×10^{-9}
MoS ₂ with Sb ₂ O ₃ and gold	3.88×10^{-8}	1.10×10^{-8}	1.86×10^{-8}	5.50×10^{-9}

4.3 Cryogenic High Vacuum Bushing Experiment

Preliminary Experiment

To demonstrate the capabilities of the cold thermal vacuum bushing tribometer, an experiment of steel on steel with a vacuum compatible fluorinated grease lubricant was performed. The normal was 100 N leading to a nominal contact pressure of 1 MPa ($F_n / (2 \cdot R_s \cdot l)$) at a sliding velocity of 10 mm/sec. Friction measurements were taken over a range of temperatures (20°C to -75°C) and plotted to reveal the influence of temperature on the friction coefficient of grease. Reversal techniques are used to eliminate biases in the moment zero. For each data point on the plot, the computed friction coefficient was taken after a sliding distance of two meters. The confidence intervals shown on the plot are an indication of the standard deviation of the phase locked friction coefficient data collected at each temperature.

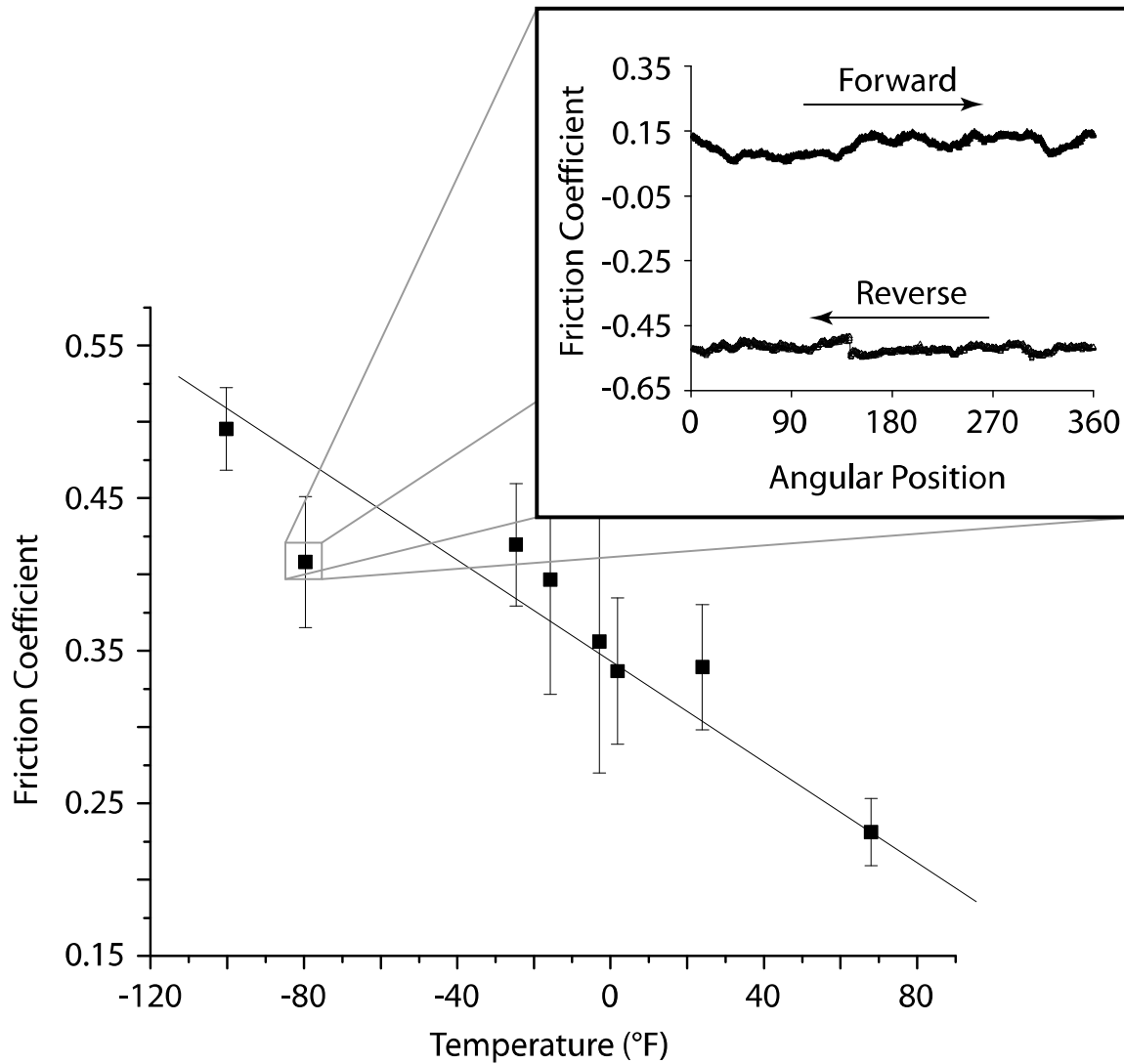


Figure 4-9 Initial experiment using fluorinated grease in a high vacuum cryogenic friction experiment.

Solid Lubricant Coating Results

Running an experiment in an application specific geometry under actual loads and sliding speeds was the initial intent of this project. In these experiments, three coatings were chosen representing the most temperature sensitive, the least temperature sensitive and an intermediate sensitivity. The tests were begun at room temperature and the temperature was ramped down to -60°C and back to room temperature throughout the course of the experiment.

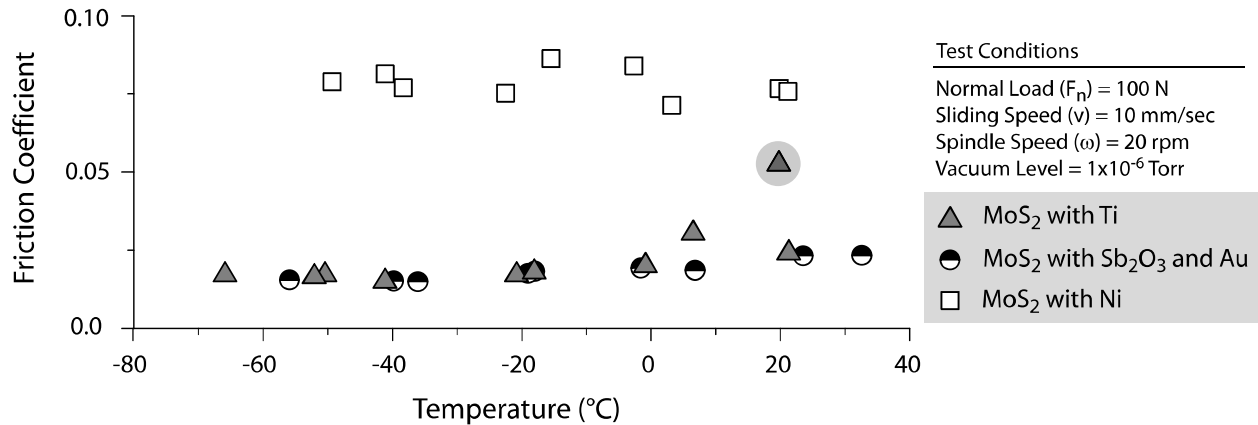


Figure 4-10 Plot of the friction response for all three coatings tested in the experiment. None of the coatings demonstrated an increase in friction with decreasing temperature in this geometry. The highlighted outlier in the MoS₂ with titanium data set was the last data point and could indicate the onset of failure for the coating. Many of these coatings failed after only a few hundred to one-thousand cycles.

The plot shows the friction of all the coatings remained low and constant for the length of the experiments. The friction coefficient values for all the coatings are consistent with values found in the cryogenic pin-on-disk experiments. One explanation for the flat friction response could be high wear rates in the bushing shaft geometry. In the linear reciprocation experiments, the coatings lasted over 10,000 cycles in all cases. However, in a bushing-shaft configuration the coating life was often shorter than 2,000 cycles indicating this geometry may be more severe tribologically. There is some discussion over whether the shaft is riding on an edge of the bushing or if the system is very axis-symmetric. The wear rate can be estimated using both assumptions to determine a possible range for the system. In an ideally aligned system where the shaft contacts the bushing across the entire length of the bushing, the wear rate is estimated at $5 \times 10^{-6} \text{ mm}^3/\text{Nm}$. If the system is running on an edge and only a small portion of the shaft is in contact, the wear rate of the system is $1.55 \times 10^{-8} \text{ mm}^3/\text{Nm}$. This range of values encompasses most of the data from the in situ wear experiments; however, it is not possible to determine if debris generated inside the contact are playing a role in lubricating the contact prior to failure.

CHAPTER 5 DISCUSSION

The term activation energy was introduced by Svante Arrhenius in 1889 to define the potential energy barrier that had to be overcome before a chemical reaction could take place. While the potential energy barrier for a reaction does not change as a function of temperature, the distribution of energy states that each atom or molecule may widen with increasing temperature. With higher temperatures, it is increasingly likely to find an atom with suitable energy to overcome the barrier and reach a more stable configuration. A schematic of the Boltzmann distribution for three temperatures is shown in figure 5-1. This helps to illustrate the effect temperature has on the system and explains why activated processes occur more readily at higher temperatures. The example of a chemical reaction is typical when discussing thermal activation, but there are other phenomena that demonstrate temperature sensitivity. Some common examples are viscoelastic creep, grain growth and diffusion of an impurity. The last of these, diffusion of an impurity (interstitial atom) through the lattice structure of another material is a well documented thermally activated process. It occurs because the atoms are vibrating at very high frequencies 10^{13} Hz or higher, and an interstitial atom will make a jump from one site to another if the orientation of the surrounding atoms is such that it can make the transition based on its kinetic energy. The amplitude of the vibrations of surrounding atoms, as well as the kinetic energy of the interstitial atom, are dominated by the temperature of the system. As the temperature of the system increases, the oscillations of lattice atoms takes them further from the average position allowing an interstitial atom to squeeze through more easily. This is discussed

in greater detail by Porter and Easterling in Phase Transitions in Metals and Alloys.(53)

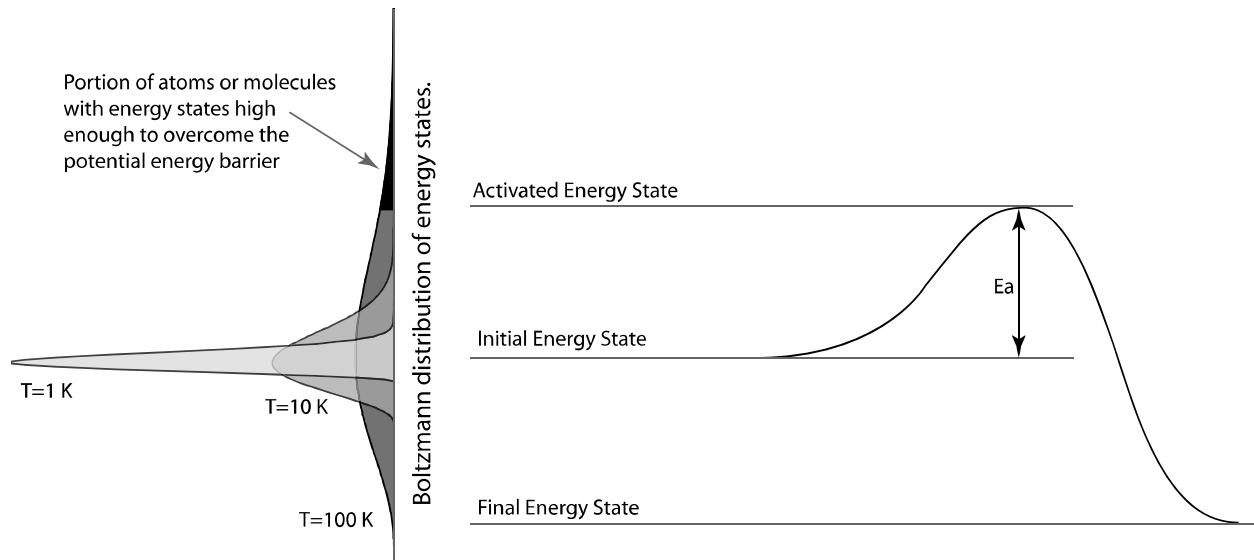


Figure 5-1 Illustration of a potential energy barrier typically found in activated chemical processes. The image to the left of the energy curve is a representation of Boltzmann energy distribution for a large number of atoms or molecules in a system at different temperatures. The portion highlighted in black is the area of the curve containing atoms with energies high enough to overcome the potential energy barrier.

As mentioned before, a previous publication on the friction response of PTFE coatings initiated these tests. In those experiments, an exponential was used to fit the results. The results in these experiments seemed to follow a similar trend. The Arrhenius equation was used to attempt to fit the data. The general form of this equation is shown in (5-1).

$$k = A \cdot e^{\frac{-E_a}{RT}} \quad (5-1)$$

In this equation, k is the rate coefficient, A is a constant, E_a is the activation energy, R is the universal gas constant and T is the temperature in Kelvin. The friction response of the coatings was modeled using this equation in the form shown in (5-2).

$$\mu = \mu_0 e^{\frac{E_a}{R} \left(\frac{1}{T} - \frac{1}{T_0} \right)} \quad (5-2)$$

Here, μ is the expected friction coefficient at temperature T , μ_0 is the room temperature friction value, the activation energy is represented by E_a , R is the universal gas constant and T_0 is room

temperature in Kelvin. In order to isolate activation energy from the other variable (room temperature friction coefficient), the friction coefficients are normalized by the room temperature value.

$$\frac{\mu}{\mu_0} = e^{\frac{E_a}{R} \left(\frac{1}{T} - \frac{1}{T_0} \right)} \quad (5-3)$$

A logarithmic transformation is used to create a linear equation in terms of activation energy.

This equation can be fit using a least squares regression analysis.

$$\ln \left(\frac{\mu}{\mu_0} \right) = \frac{E_a}{R} \left(\frac{1}{T} - \frac{1}{T_0} \right) \quad (5-4)$$

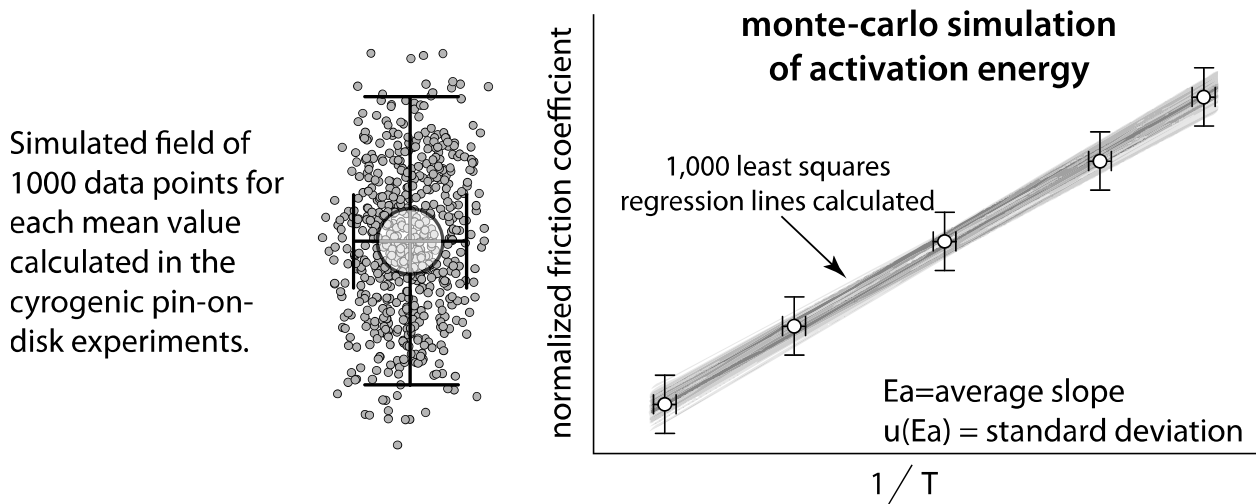


Figure 5-2 Illustration of methodology for creating a Monte Carlo simulation of activation energies.

The plot of the raw friction data for MoS₂ with Sb₂O₃ and the transformed data can be seen in figure 5-2. Because there are only four data points for each curve, it is difficult to determine an uncertainty in the fit directly. The line represented in figure 5-3(a) and 5-3(b) was determined using a linear regression technique combined with a Monte Carlo style of simulation. This style of analysis uses the mean values for each data point (μ and T), shown as circles in figure 5-3, as

the central value in the simulation and generates a number of alternative values, in this case 1,000, that could also be reasonable given the standard deviation calculated from the raw data.

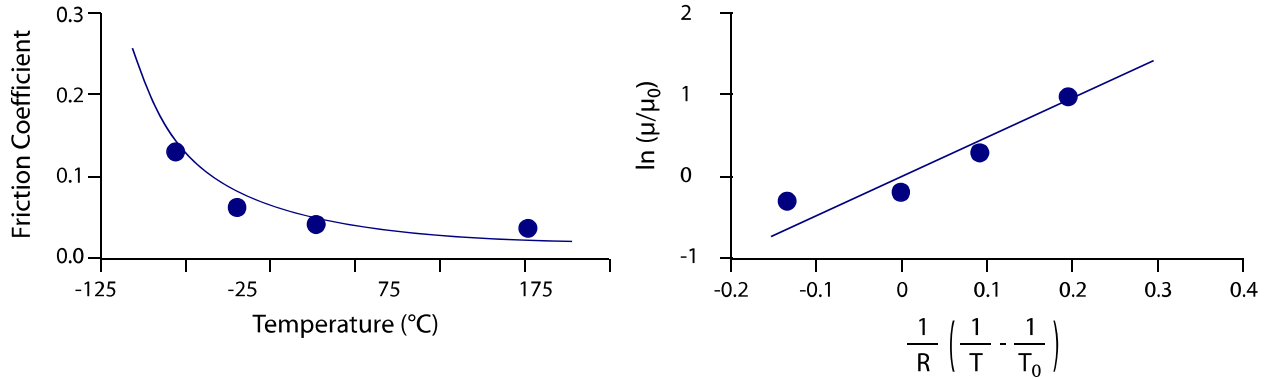


Figure 5-3 One data series in standard and logarithmic plot with fit. (a) Example of raw friction data with fit of the data. (b) Transformed data with plot of fit. This format is used to generate a fit using least squares regression.

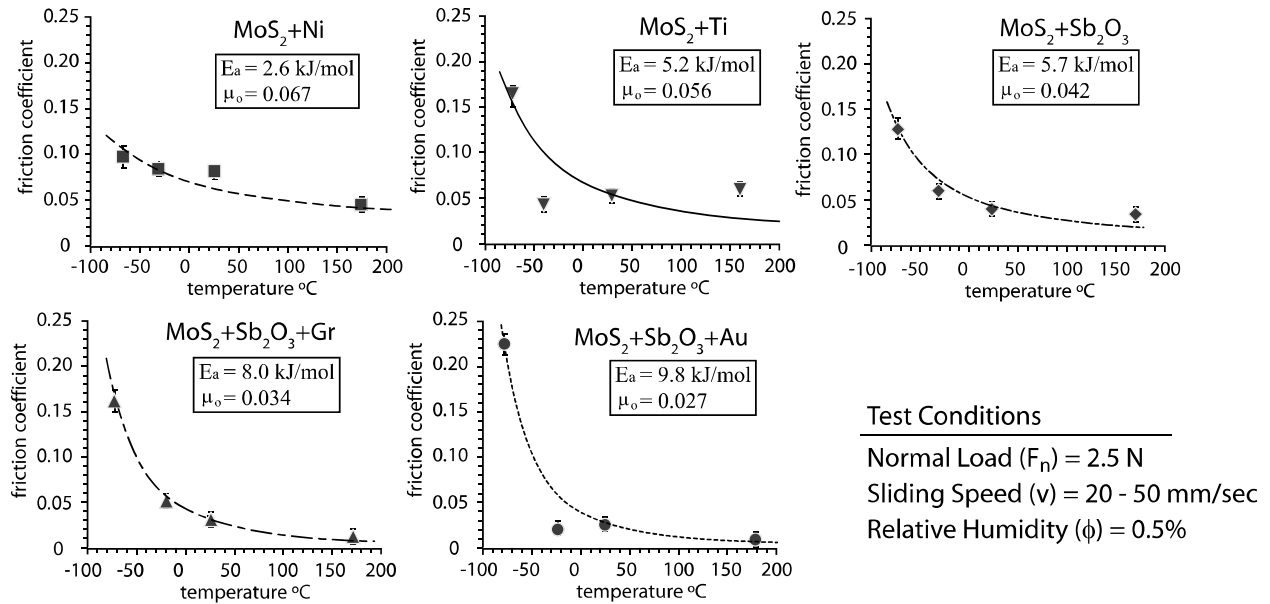


Figure 5-4 Activation energy fits for all the MoS₂-based composite coatings. This value can be thought of as a thermal sensitivity for the coating.

For each of the alternative data series, the room temperature friction coefficient and activation energy are calculated. The mean value of all the fits is the reported activation energy,

and the standard deviation of these values is reported as the uncertainty in activation energy. In many cases, the spread of the data was sizeable, but the resulting uncertainty in the fit was not.

Table 5-1 Activation energy values from Monte Carlo simulations of all the data along with the uncertainties in those values.

Coating Material	μ_0	Ea (kJ/mol)	u(Ea) (kJ/mol)
MoS ₂ with nickel	0.074	1.93	0.45
MoS ₂ with Sb ₂ O ₃	0.042	5.66	0.41
MoS ₂ with titanium	0.056	4.09	0.99
MoS ₂ with Sb ₂ O ₃ and graphite (deposited)	0.033	8.18	0.60
MoS ₂ with Sb ₂ O ₃ and gold	0.030	9.50	0.55

The friction results for the MoS₂-based coatings in a pin-on-disk configuration show something about these systems is thermally activated. The increase in friction coefficient with decreasing temperature varied based on the coating composition. Initially, the hypothesis was that increasing the amount of MoS₂ in the coating was decreasing the temperature sensitivity. However, after testing several compositions ranging from 50% MoS₂ to 95% MoS₂, there was not a strong correlation.

As mentioned before, there was a noticeable difference in the depth of the wear scars and the appearance of wear debris from one coating to the next. The wear rate values determined in the *in situ* wear experiments offered on plausible explanation for the activation energy. By plotting the of activation energy vs. wear rate for each of the coatings, a correlation between the two was revealed.

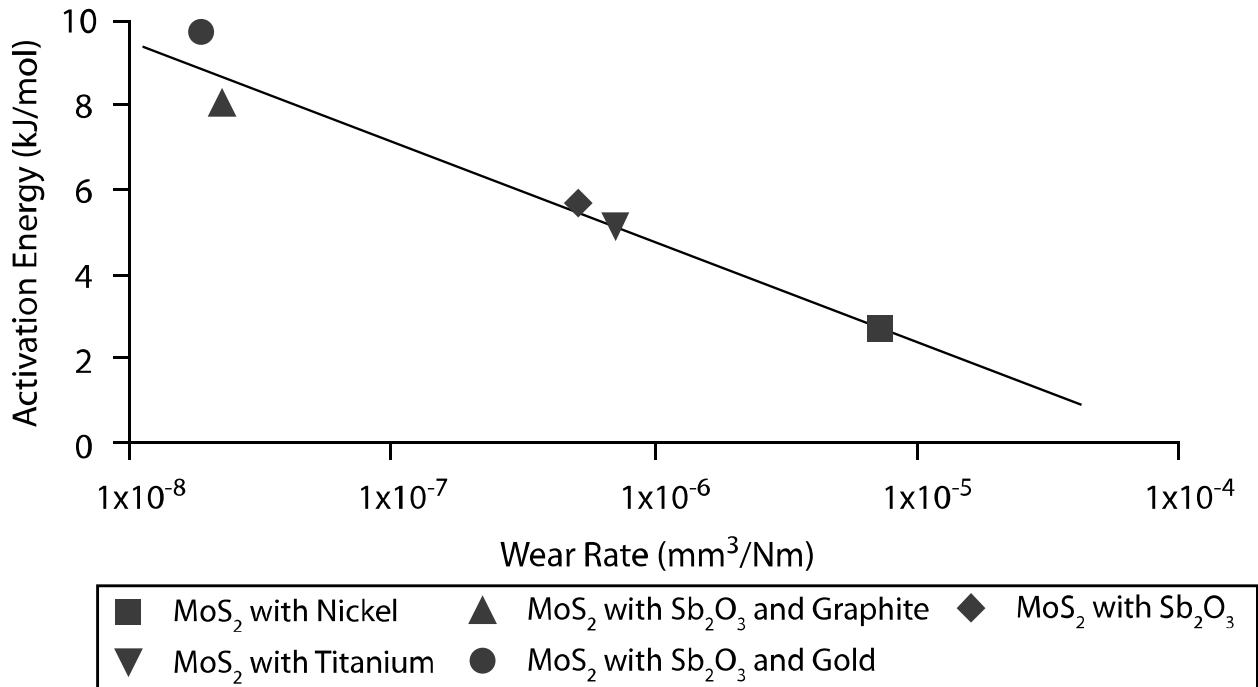


Figure 5-5 Plot of activation energies determined from the cryogenic testing of all the MoS₂ coatings as a function of wear rate determined by the in situ experiments for the same coatings.

The MoS₂ with nickel had the highest wear rate of all the MoS₂ composite coatings. The wear scar on this film grew beyond the field of view of the SWLI after 7,000 sliding cycles meaning that wear volumes could not be calculated beyond that point. This sample also had the lowest sensitivity to temperature (1.93 kJ/mol). The MoS₂ with Sb₂O₃ and gold wore only one hundred nanometers over the course of 10,000 cycles leading to the lowest wear rate of all the coatings tested. This coating also had the highest activation energy of all the coatings (9.5 kJ/mol). As indicated in the plot, there is a trend of decreasing wear rate with increasing activation energy. The link between these two properties seems to be interfacial sliding. During interfacial sliding, the interaction between surfaces is dominated by van der Waals forces. In the MoS₂ films, the lamellar structure results in planes of the molecule that form sheets with strong bonds. Between these sheets the sulphur atoms interact creating a weak van der Waals bond

resulting in low shear strength for the material. The commonly used analogy for this coating is the deck of cards explanation. The layers of MoS₂ act like a deck of cards which can be sheared easily.

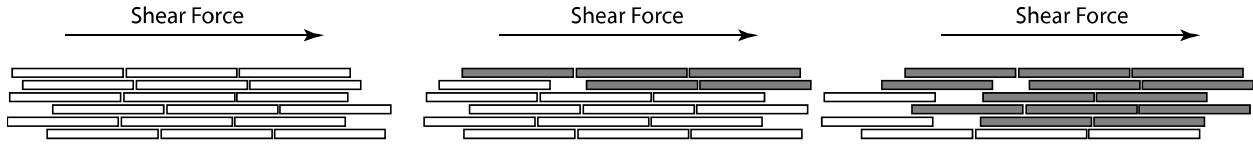


Figure 5-6 The deck of cards illustration for sliding between lamellar MoS₂ sheets. The interfaces that are shearing change throughout the sliding event, but the shear force does not change.

In this low shear strength configuration, the only interactions between sheets of MoS₂ are van der Waals type interactions. It is hypothesized that van der Waals interactions are temperature sensitive due to a blurring of the potential surface as the temperature of the system increases. This occurs in a manner similar to that outlined in figure 5-1.

Another interesting result was the increase in wear rate as the MoS₂/titanium system was cycled from a dry nitrogen environment to a humid air environment. This is perhaps due to a large area of the surface covered with nascent MoS₂ that formed during sliding in a dry environment. This nascent MoS₂ likely oxidized when oxygen was reintroduced to the system causing a large amount of debris generation and an increase in wear volume. The reaction of MoS₂ with O₂ is a spontaneous one defined by the following equation.



This reaction has a negative change its Gibbs free energy of 2,249 kJ/mol at room temperature (calculations for all chemical reactions can be found in Appendix D). Initially, the theory was the water in the system caused the degradation; however, free energy calculations found in appendix D indicate water will not spontaneously react with MoS₂. The untested surfaces are

likely covered with oxides formed after the sample was created, so running in a humid environment would not cause such a dramatic increase in the wear rate. By sliding in a dry environment all the oxides formed on the surface are removed initially leaving a low friction low wear interface to accommodate the remaining cycles. The uncovered MoS₂ would be much more reactive to oxygen causing the surface to oxidize and degrade quickly.

CHAPTER 6 CONCLUSIONS

- Three high-vacuum tribometers were designed and constructed to test samples in a variety of environments and contact geometries.
- The variable temperature pin-on-disk experiments indicated an increase in friction coefficient with decreasing temperature.
- There was a strong correlation between activation energy and wear rates for the MoS₂-based coatings.
- The cryogenic bushing tribometer experiment support a hypothesis that if the tribological contact is dominated by surface deformation and wear, there will be no sensitivity to temperature variations. The wear rate in this system cannot be directly measured, but because the system fails after roughly 1,000 cycles, it is a high-wear system.

CHAPTER 7 FUTURE DIRECTIONS

Cryogenic high vacuum linear reciprocating tribometer experiments are in the immediate future for this project. As mentioned in chapter 2, this tribometer is the easiest to fit with cryogenic cooling capabilities and resistive heating capabilities; making it an obvious choice for continuing to evaluate the temperature response of materials. This system has the best chance of answering the question of why a pin-on-disk experiment in dry nitrogen displayed a strong temperature dependence and a high vacuum bushing geometry did not. Wear measurements can be made for this system using the SWLI before the experiment and after the experiment giving a clear value for volume loss.

The in situ wear experiments proved helpful at determining the behavior of these systems to environmental changes. There are also many improvements to the technique that can be made to increase the quality and consistency of the data collected. The first step that can be taken in future experiments is to have the SWLI take several surface scans of an image and average over them to improve the repeatability of the scans. Using a single scan, the repeatability of the measurements was 40nm. The uncertainty of the scans is reduced to 10nm by averaging five surface scans. This improvement helps eliminate surface noise in the system which is readily apparent in the line scans used to calculate wear volumes. A second area for improvement is the calculation of wear volumes. Extrapolating a single line over the entire length of the wear scar can skew the results, particularly if a piece of debris falls into the area where the line scan is being taken. Finding a wear volume based on the entire surface scan (usually several hundred microns in both directions) can give a better representation of the scar. One method for calculating this value is to use the entire initial surface scan as the undeformed surface and find

the difference between that and a subsequent scan. This should help to eliminate the influence of noise in the scan and debris on the surface.

Another direction is in the use of molecular dynamics simulations to evaluate the potential surfaces for model system at different temperatures. This analysis could provide insight as to why temperature effects are very dramatic in the low temperature regimes and tend to fall off as the temperature is increased. One theory is the corrugation of the potential surface becomes blurred as the temperature increases reducing the driving forces necessary to cause shear in the solid lubricant interface. Careful evaluation of the potential surfaces at varying temperatures could shed light on this theory.

APPENDIX A
UNCERTAINTY ANALYSIS OF FALEX POD TRIBOMETER

The uncertainty of the friction coefficients measured by the Falex tribometer can be quantified using the law of propagation of uncertainty. In this case, there are several contributing factors in the uncertainty of the friction coefficient. They are:

- Mass of the dead weight load (m)
- Ratio of lengths from the dead weight load to the gimbal and the pin contact to the gimbal (R2).
- Ratio of lengths from the friction transducer to the gimbal and the pin to the gimbal (R3).
- Friction force measured by the strain gauge (Fs).

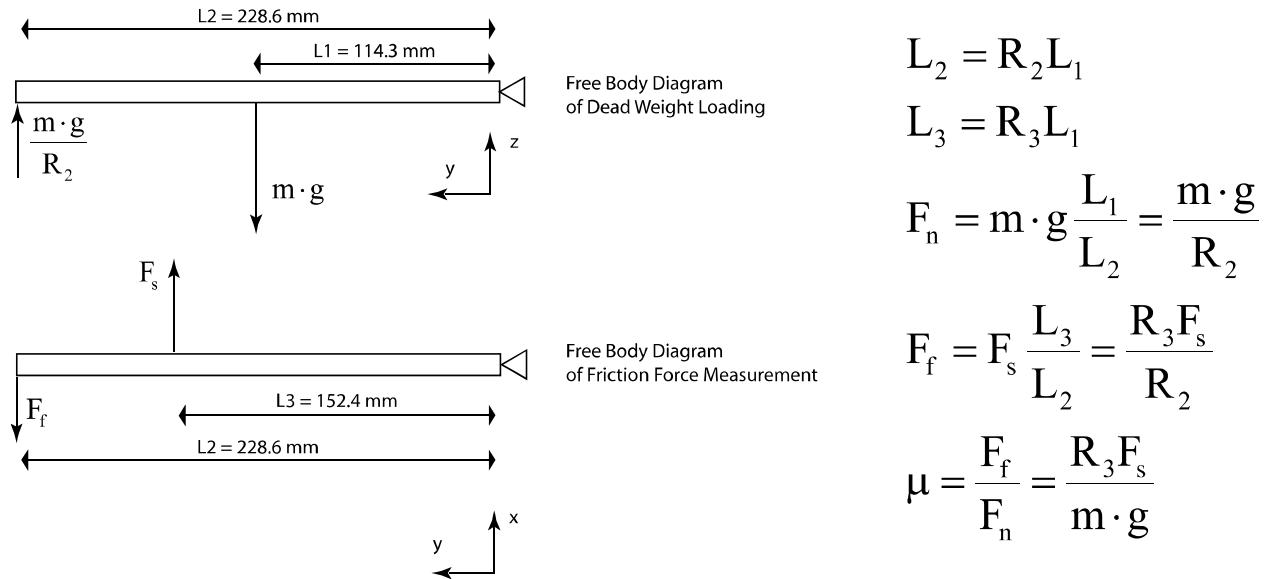


Figure A-1 Free body diagram of Falex pin-on-disk tribometer with friction coefficient calculations.

The normal load applied to the sample is calculated based on the ratio R2 and the mass of the dead weight load.

$$F_n = \frac{m \cdot g}{R_2} \sim \frac{m \cdot g}{2}$$

The law of propagation of uncertainty indicates the uncertainty of this measurement to be:

$$u(F_n)^2 = \left(\frac{\partial F_n}{\partial m}\right)^2 u(m)^2 + \left(\frac{\partial F_n}{\partial R_2}\right)^2 u(R_2)^2$$

$$u(F_n)^2 = \left(\frac{g}{R_2}\right)^2 u(m)^2 + \left(\frac{-m \cdot g}{R_2^2}\right)^2 u(R_2)^2$$

$$u(F_n)^2 = \left(\frac{9.81}{2.0}\right)^2 (5 \times 10^{-4})^2 + \left(\frac{-0.5 \cdot 9.81}{4.0}\right)^2 (0.05)^2$$

$$u(F_n) = 0.062$$

The uncertainty of the friction force can also be calculated using the law of propagation of uncertainty:

$$F_f = \frac{F_s \cdot R_3}{R_2}$$

$$u(F_f)^2 = \left(\frac{\partial F_f}{\partial F_s}\right)^2 u(F_s)^2 + \left(\frac{\partial F_f}{\partial R_2}\right)^2 u(R_2)^2 + \left(\frac{\partial F_f}{\partial R_3}\right)^2 u(R_3)^2$$

$$u(F_f)^2 = \left(\frac{R_3}{R_2}\right)^2 u(F_s)^2 + \left(\frac{-F_s \cdot R_3}{R_2^2}\right)^2 u(R_2)^2 + \left(\frac{F_s}{R_2}\right)^2 u(R_3)^2$$

$$u(F_f)^2 = \left(\frac{1.33}{2.0}\right)^2 (0.01)^2 + \left(\frac{-0.05 \cdot 1.33}{4.0}\right)^2 (0.05)^2 + \left(\frac{0.05}{2.0}\right)^2 (0.05)^2$$

$$u(F_f) = 0.011$$

The friction coefficient uncertainty value can now be calculated using the uncertainties of its constituents.

$$\mu = \frac{F_f}{F_n}$$

$$u(\mu)^2 = \left(\frac{\partial \mu}{\partial F_f}\right)^2 u(F_f)^2 + \left(\frac{\partial \mu}{\partial F_n}\right)^2 u(F_n)^2$$

$$u(\mu)^2 = \left(\frac{1}{F_n}\right)^2 u(F_f)^2 + \left(\frac{-F_f}{F_n^2}\right)^2 u(F_n)^2$$

$$u(\mu)^2 = \left(\frac{1}{2.5}\right)^2 (0.011)^2 + \left(\frac{-0.05}{6.25}\right)^2 (0.062)^2$$

$$u(\mu) = 0.007$$

Although the calculated uncertainty of the system is 30% of the measured value at $\mu = 0.02$, the electronics used to output the data to the data acquisition system report friction coefficient as a voltage. The resolution of the system is 1 mV corresponding to a friction coefficient of 0.001; a conservative estimation of the uncertainty of the electronics is 10 mV corresponding to a friction

coefficient of 0.01. This value will be used as the uncertainty in the measurements for all the data in the pin on disk experiments.

APPENDIX B HIGH VACUUM PIN-ON-DISK EXPERIMENT

Environmental Protocols

The high vacuum experiments were meant to evaluate the friction response of the coatings when run in ambient air (relative humidity ~ 40%) and high vacuum (pressure < 1×10^{-6} Torr). The first test procedure was to run one track from each sample in ambient air then a second track at high vacuum. The load used in these tests was 5 N. This value was chosen so coatings with a low friction coefficient (below 0.05) would still generate a friction force large enough to provide reasonable certainty in the measurement. These experiments were all run at ambient temperature ($T \sim 23^\circ\text{C}$). The sliding speed for these experiments was approximately 20 mm/sec regardless of track diameter. This was made possible by the precise spindle control of high vacuum motor.

A second procedure was also used with the high-vacuum pin-on-disk testing referred to as 'pump and purge'. In these tests, the sample was mounted in the pin-on-disk, the chamber was evacuated to high vacuum and the motor was started. After the sample ran in to steady-state in high vacuum, the chamber was opened to ambient air at 40% relative humidity. Once the pressure equilibrated the system was allowed to run to a steady-state condition before the chamber was evacuated again. These tests were performed to see if cycling environments had any effect on the friction response of the coatings.

Experimental Procedure

Although the high vacuum pin-on-disk tribometer has multiple sample holders to allow for a variety of disk diameters, all the samples used in this experiment are 2" diameter 1/4" thick disks and 1/4" diameter balls. The disk sample was placed on the sample mount bolted to the face of the motor. The cover plate was screwed down over the disk pinching it in place. This design holds the disk flush to the surface and prevents it from moving during the test. As with the disk holders, there are multiple pin flexures to accommodate different diameter pin samples. The 1/4" sample is inserted into the holder and a set screw is tightened behind the ball holding it firmly in the housing and preventing it from slipping during the experiment. The sample flexure is attached to the load cell assembly, and the load cell is tared. This ensures all forces exerted on the pin sample are accurately read by the transducer. LabView is started and the program written for this tribometer is executed. The calibration constants for the load cell, pressure gauge and thermocouples are entered into the software. The location where the data files are to be saved is chosen and the program waits for the user to begin data acquisition. The micrometer stage where the load cell assembly is attached is adjusted to the desired track radius for the experiment. Once positioned, a second micrometer stage is adjusted to bring the sample into contact and apply a normal load. The normal force is read in real-time within the LabView software. When the appropriate load has been applied, the chamber is closed and the system pumped down to the target vacuum level for the experiment. The data acquisition is started in the LabView software which subsequently commands the motor to begin. Average values for ambient pressure, normal force and friction force are recorded throughout the experiment and appended to an average data file for post processing. Periodically, one complete revolution of data is recorded.

Humid Air and High Vacuum Testing

The sensitivity of MoS₂ based coatings to humidity is well documented. Water contaminates the lamellar structure of MoS₂ increasing the stress required to shear the material. In a solid lubricant coating, this contamination results in an increased friction coefficient. The expectation for the high vacuum pin-on-disk experiments was that the MoS₂ based coatings would be extremely sensitive to the partial pressure of water in the system. In metallic coatings, the friction force tends to be dominated by abrasive wear and plastic deformation; there is no indication that the presence of humidity would improve the ability of these materials to mechanically deform. The polymeric systems, being chemically inert, were also expected to be insensitive to humidity. The table below shows all the pin-on-disk results for high vacuum and humid air.

Table B-1 Summary of results from high vacuum pin-on-disk tribometer in humid laboratory air and high vacuum. All tests were run at a normal load of 5N and a sliding speed of 20 mm/sec.

Coating Material	Friction Coefficient	
	Air	High Vacuum
Hard anodized aluminum	0.75	0.88
Hard anodized aluminum with PTFE	0.13	0.12
Titanium nitride with electroless nickel	0.65	0.61
MoS ₂ with Sb ₂ O ₃ and graphite (burnished)	0.16	0.01
MoS ₂ with Sb ₂ O ₃ and graphite (deposited)	0.13	0.05
MoS ₂ with titanium	0.12	0.01
MoS ₂ with nickel	0.27	0.02
PTFE with PEEK and MoS ₂	0.12	0.1
UHMWPE	0.05	0.03
Near frictionless carbon	0.05	0.008

As expected, the metallic coatings did not display much sensitivity to humidity in the environment. In all cases, the metallic coatings showed little change compared with the scatter in the data from these systems. The MoS₂ coatings showed dramatic decreases in friction coefficients in high-vacuum. Again, this result was not surprising. The unexpected results was in the polymeric systems which displayed decrease in friction response when humidity was removed from the system. Given the chemical inertness of these systems, it was hard to determine what caused this change. However, more recent work in this field has indicated there is a sensitivity to water for PEEK composites.(54)

Pump and Purge Test Results

The other test outlined in the experimental procedures section was the ‘pump and purge’ experiment. The importance of this experiment was to determine if repeated cycling of the

environments had any effect on the friction response of the materials. To evaluate this, two different samples were chosen, the MoS₂ with titanium coating and a bulk polymer composite of PTFE with PEEK and MoS₂. Both of these samples were run in alternating environments to determine the effects of cycling the environment. The figure below illustrates the results for each sample.

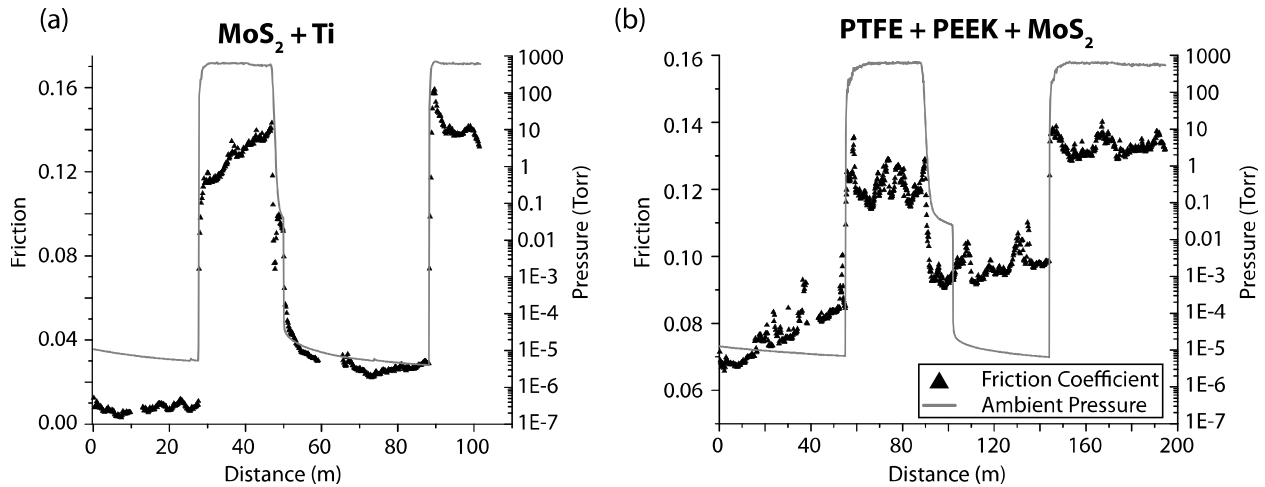


Figure B-1 Pump and purge data results for a thin coating and bulk polymer. (a) MoS₂ with titanium and (b) PTFE with PEEK and MoS₂

In both cases, the material began at high vacuum and was exposed to humid air then the cycle was repeated. The samples displayed a similar response, although the MoS₂ with titanium was much more dramatic, both saw the lowest friction under high vacuum in the initial cycles. The friction immediately increased upon exposure to humid air, and after pumping the system back down, the friction did not recover to its initial value, indicating some oxidation or permanent deformation of the system occurred while running in a humid environment. In the polymer experiment, it appears the system did not reach an equilibrium state prior to swapping the environment. The friction was clearly affected by the humidity in the system, but it is not possible to determine the extent of the change as the friction seems to be increasing continually during the experiment. One possible explanation for this is a continual deformation of the surface throughout the test due to the high contact pressures. This results in a more conformal contact, a larger real area of contact and ultimately higher friction forces.

APPENDIX C
AUGER ELECTRON SPECTROSCOPY OF COATINGS

Of the coatings tested, two were chosen to have Auger electron spectroscopy performed on them. These were the MoS₂ with titanium coating, mainly because it is designed to be environmentally insensitive, and the MoS₂ with Sb₂O₃ and graphite, because this coating is designed to rely on different constituents to provide solid lubrication in differing environments. The samples used were from the 10,000 cycle single environment experiments. Two tracks were used for each sample; the first was run in humid air for 10,000 cycles and the second in dry nitrogen for 10,000 cycles. In each case, a line scan was performed across the track evaluating different elements. The MoS₂ with titanium samples were checked for carbon, molybdenum, oxygen, sulphur and titanium. The MoS₂ with Sb₂O₃ and graphite was tested for carbon, molybdenum, oxygen, sulphur and antimony. In all four systems there were distinctly different signatures. The data shown in all the plots are the normalized intensities for each element. This was chosen because some elements are more likely to emit Auger electrons than others skewing the raw data. Sulphur, for example, is one of the elements most likely to emit an Auger electron, so its intensity dominates most of the scans. By normalizing the data, it is possible to look at the intensities of all the atoms inside and outside the tracks more easily.

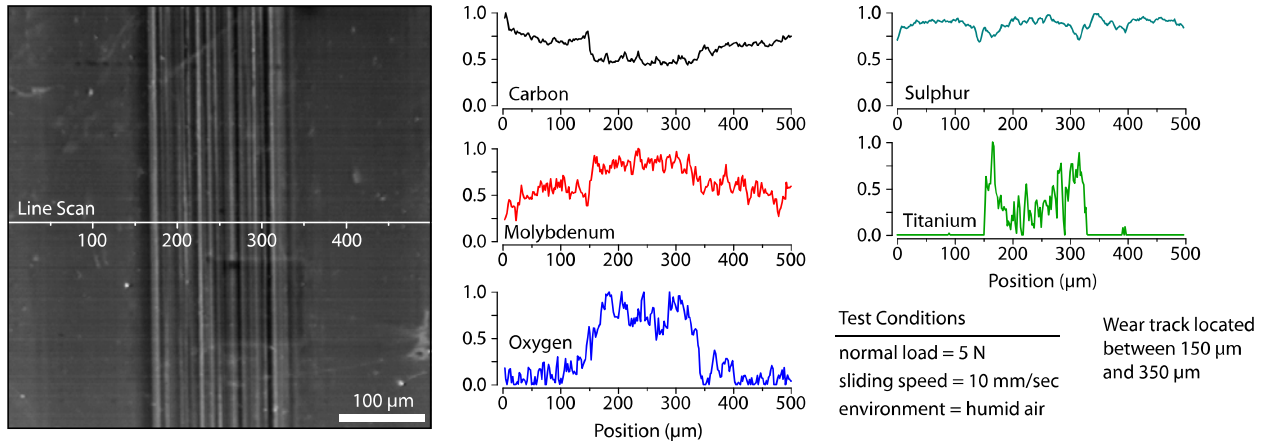


Figure C-1 Relative intensities for several elements plotted vs. position across the wear track for the MoS₂ with titanium coating run in humid air environment. Auger data indicates a high content of titanium and oxygen (likely titania) on the surface inside the wear track. The signature of the other elements was relatively constant inside and outside the track.

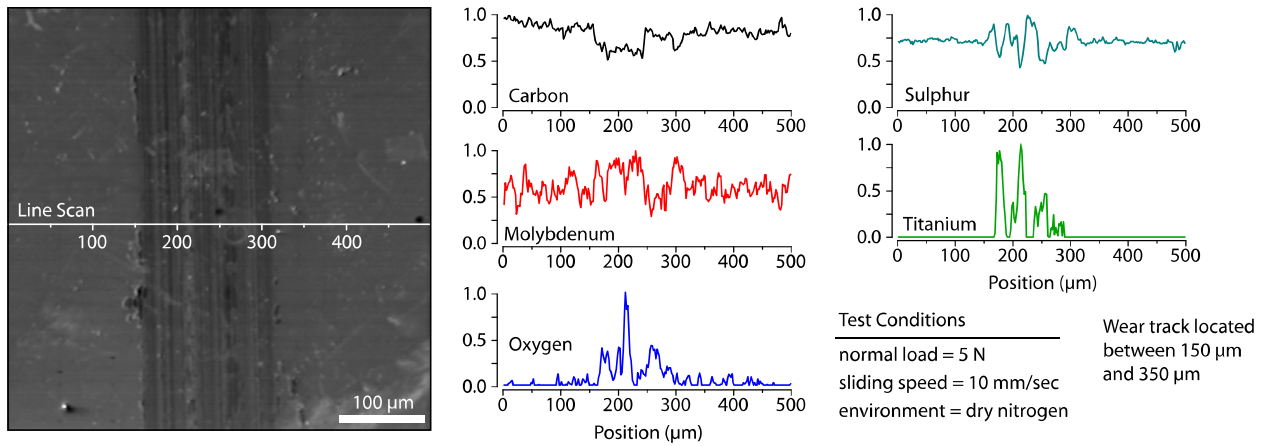


Figure C-2 Relative intensities for several elements plotted vs. position across the wear track for the MoS₂ with titanium coating run in dry nitrogen. Like the humid air data, dry nitrogen data indicates a higher content of titanium and oxygen (likely titania) on the surface inside the wear track. However, there are also distinct changes in the sulphur and molybdenum signatures inside the track indicating more MoS₂ is on the surface.

The MoS₂ with titanium coating had a distinct signature for titanium and oxygen inside the wear track in both humid air and dry nitrogen. This indicates titania is being formed in the system as the track is worn in. The signals from molybdenum and sulphur remained constant across the track indicating there was still a reasonable amount of MoS₂ remaining in the track. The track run in dry nitrogen did have an increase in titanium and oxygen inside the track, but there was also an increase in sulphur. While the environment is dry nitrogen, there are always impurities present. These results indicate any oxygen in the environment seems to be trapped by the titanium in the coating, but the presence of titania does not impede the MoS₂ and may help to prevent its oxidation.

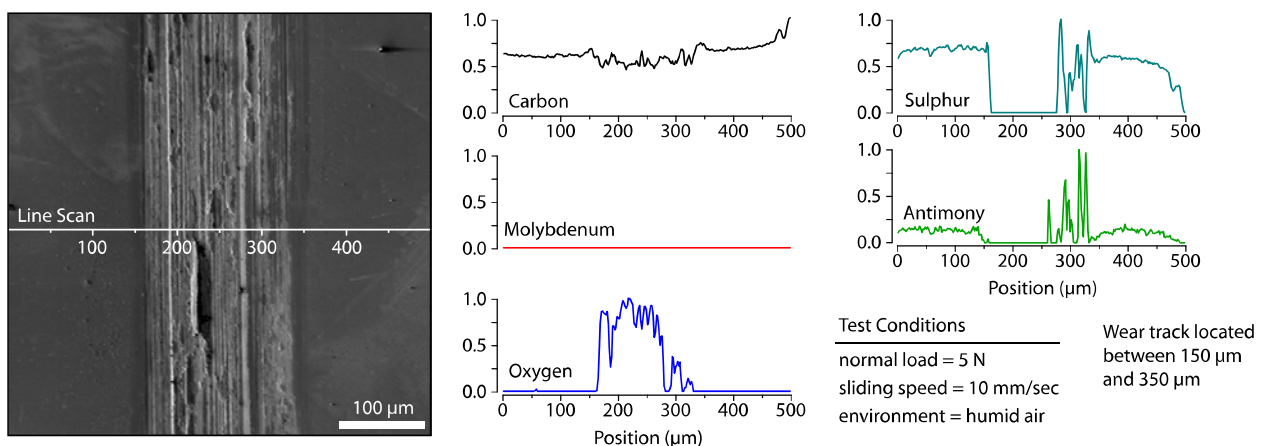


Figure C-3 Relative intensities for several elements plotted vs. position across the wear track for the AFRL chameleon coating run in humid air. There is no signal from the molybdenum in this coating. Oxygen and carbon are primarily found inside the wear track while sulphur and antimony are depleted inside the track.

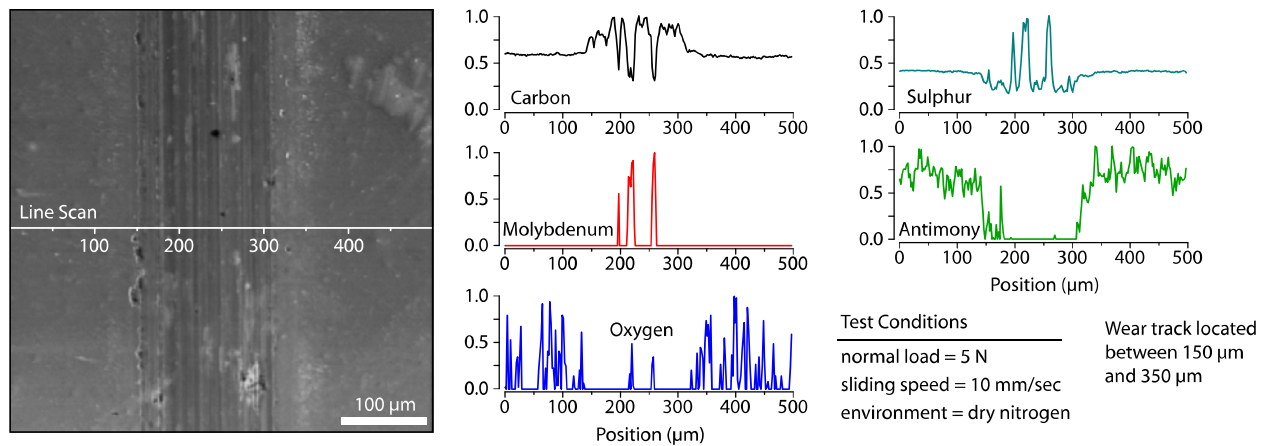


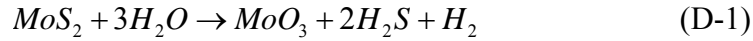
Figure C-4 Relative intensities for several elements plotted vs. position across the wear track for the AFRL chameleon coating run in dry nitrogen. The molybdenum, sulphur and carbon intensities increase inside the wear track. The difference between this scan and the open air tests indicate MoS_2 is, in fact, drawn to the surface of the coating during wear.

The MoS_2 with Sb_2O_3 and graphite results indicated that the coating does have a stronger signal from MoS_2 on the surface running in dry nitrogen as opposed to humid air. The humid air results indicated mostly carbon and oxygen in the wear track. This result is expected based on the hypothesis that the preferred solid lubricant is drawn to the surface. The lack of a signal from molybdenum and the sharp decrease in sulphur signal inside the wear track also confirm that carbon (could be graphitic), not MoS_2 , is the primary constituent on the surface of the material after running in a humid environment.

APPENDIX D
GIBBS FREE ENERGY CALCULATIONS

The oxidation of MoS₂ to MoO₃ is a process of importance in this study. Determining which species are primarily involved in the reaction is key to predicting when it will occur. To that end, the two species present in humid air that are known to react with a variety of materials, Oxygen and water were evaluated as causes for oxidation.

A chemical reaction involving water and MoS₂ is listed below. This equation is generated solely by balancing the reactants with the products.



For this chemical reaction to occur spontaneously the Gibbs free energy of the system must be less than 0 kJ/mol. The reaction is assumed to occur at room temperature 298K. The values for enthalpy and entropy for each species is listed in the table below.

Table D-1. List of values for enthalpy and entropy for species in (D-1).(55)

Species	Enthalpy	Entropy
MoS ₂	-276 kJ/mol	63 J/mol-K
H ₂ O	-242 kJ/mol	189 J/mol-K
MoO ₃	-745 kJ/mol	78 J/mol-K
H ₂ S	-21 kJ/mol	206 J/mol-K
H ₂	0 kJ/mol	131 J/mol-K
O ₂	0 kJ/mol	205 J/mol-K
SO ₂	-297 kJ/mol	248 J/mol-K
H ₂ SO ₄	-735 kJ/mol	299 J/mol-K

To calculate the free energy of the equation, the value can be found using equation D-2.

$$\Delta H + \Delta S \cdot T = G \quad (D-2)$$

The value for the reaction listed in D-1 is calculated as follows:

$$\begin{aligned} & \left(H_{MoO_3} + 2H_{H_2S} + H_{H_2} \right) - \left(H_{MoS_2} + 3H_{H_2O} \right) + \\ & \frac{T}{1000} \left[\left(S_{MoO_3} + 2S_{H_2S} + S_{H_2} \right) - \left(S_{MoS_2} + 3S_{H_2O} \right) \right] = G \end{aligned} \quad (D-3)$$

$$(-745 - 42 - 0) - (-276 - 726) + \frac{298}{1000} [(78 + 412 + 131) - (63 + 563)] = G \quad (D-4)$$

$$G = 205 \frac{kJ}{mol} \quad (D-5)$$

This result indicates the reaction will not occur spontaneously until the temperature is far above the decomposition temperature of the material.

Another possible reaction is that Oxygen present in the environment is causing the oxidation of the MoS₂. This reaction is defined in D-6.



Using D-2, and the values from Table D-1, the free energy of this reaction is calculated as follows:

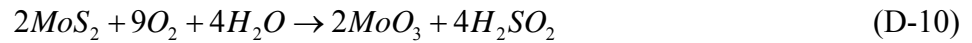
$$\left(2H_{MoO_3} + 4H_{SO_2}\right) - \left(2H_{MoS_2} + 7H_{O_2}\right) + \frac{T}{1000} \left[\left(2S_{MoO_3} + 4S_{SO_2}\right) - \left(2S_{MoS_2} + 7S_{O_2}\right)\right] = G \quad (D-7)$$

$$(-1490 - 1188) - (-552 - 0) + \frac{T}{1000} [(156 + 992) - (126 + 1435)] = G \quad (D-8)$$

$$G = -2249 \frac{kJ}{mol} \quad (D-9)$$

Because the free energy of the reaction is far below zero at room temperature, the reaction is expected to occur spontaneously.

A third reaction includes the combination of water and oxygen in the system to oxidize the MoS₂.



Using the same method from D-7 to D-9, the free energy of this reaction is calculated to be

$$G = -4177 \frac{kJ}{mol} \quad (D-11)$$

Both water and oxygen can be found in the system in all the experiments listed in this study. These results only strengthen the conclusion that further testing must be performed in vacuum where the partial pressures of every species can be accurately measured.

LIST OF REFERENCES

1. P. J. Rae, D. M. Dattelbaum, *Polymer* **45**, 7615 (Oct. 13, 2004).
2. E. N. Brown, D. M. Dattelbaum, *Polymer* **46**, 3056 (Apr. 15, 2005).
3. P. J. Rae, E. N. Brown, *Polymer* **46**, 8128 (Sep. 8, 2005).
4. E. N. Brown, P. J. Rae, E. B. Orler, G. T. Gray, D. M. Dattelbaum, *Materials Science & Engineering C-Biomimetic and Supramolecular Systems* **26**, 1338 (Sep. 2006).
5. V. Hopkins, M. Campbell, *Lubrication Engineering* **25**, 430 (1969).
6. N. L. McCook, D. L. Burris, P. L. Dickrell, W. G. Sawyer, *Tribology Letters* **20**, 109 (Oct. 2005).
7. X. Zhao, M. Hamilton, W. G. Sawyer, S. S. Perry, *Tribology Letters*, 12 (Aug. 2007).
8. A. Schirmeisen, L. Jansen, H. Holscher, H. Fuchs, *Applied Physics Letters* **88** (Mar. 20, 2006).
9. M. E. Bell, J. H. Findlay, *Physical Review* **59**, 913 (1941).
10. R. L. Johnson, D. Godfrey, E. E. Bisson, *National Advisory Committee for Aeronautics - Technical Note* (1948).
11. V. R. Johnson, G. W. Vaughn, *Journal of Applied Physics* **27**, 1173 (1956).
12. R. F. Deacon, J. F. Goodman, *Proceedings of the Royal Society of London Series a-Mathematical and Physical Sciences* **243**, 464 (1958).
13. A. J. Haltner, C. S. Oliver, *Industrial & Engineering Chemistry Fundamentals* **5**, 348 (1966).
14. W. A. Brainard, *Nasa Technical Note D-5141*, 1 (1969).
15. S. Ross, A. Sussman, *Journal of Physical Chemistry* **59**, 889 (1955).
16. W. Engelmaier, *Lubrication Engineering* **25**, 442 (1969).
17. T. Spalvins, J. Przybyszewski, *Nasa Technical Note D-4269*, 1 (Dec. 1967).
18. T. Spalvins, *Lubrication Engineering* **25**, 436 (1969).
19. I. Petrov, P. B. Barna, L. Hultman, J. E. Greene, *Journal of Vacuum Science & Technology A* **21**, S117 (Sep-Oct. 2003).

20. R. Holinski, Gansheim.J, *Wear* **19**, 329 (1972).
21. T. Spalvins, *Journal of Vacuum Science and Technology A* **5**, 212 (1987).
22. S. G. Gould, E. W. Roberts, *23rd Aerospace Mechanisms Symposium, Huntsville, AL. NASA Conference Publication 3032* (May 3, 1989).
23. B. C. Stupp, *Thin Solid Films* **84**, 257 (1981).
24. P. D. Fleischauer, R. Bauer, *Tribology Transactions* **31**, 239 (Apr. 1988).
25. J. S. Zabinski, M. S. Donley, S. D. Walck, T. R. Schneider, N. T. Mcdevitt, *Tribology Transactions* **38**, 894 (Oct. 1995).
26. A. A. Voevodin, J. J. Hu, T. A. Fitz, J. S. Zabinski, *Surface & Coatings Technology* **146**, 351 (Sep-Oct. 2001).
27. M. Suzuki, P. Prat, *Wear* **229**, 995 (Apr. 1999).
28. J. J. Nainaparampil, A. R. Phani, J. E. Krzanowski, J. S. Zabinski, *Surface & Coatings Technology* **187**, 326 (Oct 22, 2004).
29. C. C. Baker, J. J. Hu, A. A. Voevodin, *Surface and Coatings Technology* **201**, 4224 (2006).
30. C. Donnet, *Surface & Coatings Technology* **80**, 151 (Mar. 1996).
31. C. Donnet, J. M. Martin, T. LeMogne, M. Belin, *Tribology International* **29**, 123 (Feb. 1996).
32. A. A. Voevodin, T. A. Fitz, J. J. Hu, J. S. Zabinski, *Journal of Vacuum Science & Technology a-Vacuum Surfaces and Films* **20**, 1434 (Jul-Aug. 2002).
33. A. A. Voevodin, J. S. Zabinski, *Composites Science and Technology* **65**, 741 (Apr. 2005).
34. A. A. Voevodin, J. S. Zabinski, C. Muratore, *Tsinghua Science and Technology* **10**, 665 (2005).
35. A. A. Voevodin, J. S. Zabinski, *Wear* **261**, 1285 (Dec 20, 2006).
36. E. W. Roberts, *Tribology International* **23**, 95 (Apr. 1990).
37. C. Donnet, T. L. Mogne, J. M. Martin, *Surface & Coatings Technology* **62**, 406 (Dec. 1993).

38. P. D. Fleischauer, J. R. Lince, *Abstracts of Papers of the American Chemical Society* **217**, U1116 (Mar 21, 1999).
39. T. L. Schmitz, J. E. Action, J. C. Ziegert, W. G. Sawyer, *Journal of Tribology-Transactions of the Asme* **127**, 673 (Jul. 2005).
40. T. L. Schmitz, J. E. Action, D. L. Burris, J. C. Ziegert, W. G. Sawyer, *Journal of Tribology-Transactions of the Asme* **126**, 802 (Oct. 2004).
41. P. L. Dickrell *et al.*, *Journal of Tribology-Transactions of the Asme* **127**, 82 (Jan. 2005).
42. J. Andersson, R. A. Erck, A. Erdemir, *Surface & Coatings Technology* **163**, 535 (Jan 30, 2003).
43. J. F. Ohanlon, *Journal of Vacuum Science & Technology a-Vacuum Surfaces and Films* **2**, 174 (1984).
44. J. F. O'Hanlon, *A user's guide to vacuum technology* (Wiley, Hoboken, N.J., ed. 3rd, 2003), pp. XVIII, 516 s.
45. N. H. Kim *et al.*, *Wear* **258**, 1787 (Jun. 2005).
46. F. P. Incropera, D. P. DeWitt, *Fundamentals of heat and mass transfer* (Wiley, New York, ed. 5th, 2002), pp. XIX, 981 s.
47. K. L. Johnson, *Contact mechanics* (Cambridge University Press, Cambridge, 1985), pp. XI, 452 s.
48. J. C. Burton, P. Taborek, J. E. Rutledge, *Tribology Letters* **23**, 131 (Aug. 2006).
49. S. Bahadur, C. Sunkara, *Wear* **258**, 1411 (Apr. 2005).
50. J. B. Williamson, R. T. Hunt, *Proceedings of the Royal Society of London Series a-Mathematical and Physical Sciences* **327**, 147 (1972).
51. R. S. Sayles, *Tribology International* **34**, 299 (May 2001).
52. S. M. Ulam, *Adventures of a mathematician ; illustrated with photographs* (Charles Scribner's Sons, New York, 1976), pp. XI, 317 s.
53. D. A. Porter, K. E. Easterling, *Phase transformations in metals and alloys* (Chapman & Hall, London, ed. 2nd, 1992), pp. xiii, 514 s.
54. N. L. McCook, M. A. Hamilton, D. L. Burris, W. G. Sawyer, *Wear* **262**, 1511 (2007).

55. *NIST Chemistry WebBook*. P. J. Linstrom, W. G. Mallard, Eds., NIST Standard Reference Database Number 69 (National Institute of Standards and Technology, Gaithersburg MD, 20899, June 2005)

BIOGRAPHICAL SKETCH

Matthew Adam Hamilton was born January 21, 1978 in Orlando, Florida. He spent a majority of his youth in Bradenton, Florida where he attended Southeast High School. In August of 1996, he entered the University of Florida. Subsequently, the football team won its first national championship. A turning point in his academic career occurred in the year 2000, when he began doing research with Dr. W. Gregory Sawyer in the Tribology Laboratory. After earning his bachelor's degree in May 2001, Matthew continued with graduate studies in the field of tribology. Upon completing his master's degree in May 2003, he took a job with a software company in New York City. After one year, the opportunity to come back to school and complete his doctorate was presented to him by Greg Sawyer. In June 2004, Matthew was readmitted to the University of Florida. He completed his doctorate in June 2007 accompanied by another national championship for the football team and back-to-back national championships for the basketball team. With aspirations of becoming a professor, Matthew accepted a post-doctoral appointment with Dr. Robert Carpick at the University of Pennsylvania to begin in August 2007.